Carbonation of photocatalytic aluminosilicate cement composites: Evolution of self-cleaning and radiative cooling properties

Cement and Concrete Composites 152 (2024) 105626

Contents lists available at ScienceDirect

Cement and Concrete Composites

journal homepage: www.elsevier.com/locate/cemconcomp

Carbonation of photocatalytic aluminosilicate cement composites: Evolution of self-cleaning and radiative cooling properties

Daoru Liu [a,b], J.C.O. Zepper [b], Yuxuan Chen [a], Lulu Cheng [a], Qingliang Yu [a,b,*]

[a] School of Civil Engineering, Wuhan University, Wuhan, 430072, China
[b] Department of the Built Environment, Eindhoven University of Technology, 5600MB, Eindhoven, the Netherlands

ARTICLE INFO

Keywords:
Carbonation
Self-cleaning
Radiative cooling
Microstructure
Phase composition

ABSTRACT

This study aims to understand the impact of carbonation on the photocatalytic self-cleaning and radiative cooling properties of autoclaved cement composites. The composites are prepared with varying silica contents and sources, with and without alumina addition under autoclave conditions. The phase composition, microstructure, optical properties, and photocatalytic self-cleaning performance are systematically characterized and analyzed. Outdoor measurements are conducted to validate the cooling performance of the material under ambient conditions. Cracking behaviors during autoclave/carbonation treatments and the performance degradation in functionalities upon carbonation are observed. The cement/nanosilica/alumina ternary system demonstrates the best overall performance, considering productibility during autoclave curing, effectiveness, and carbonation durability of functionalities. C-A-S-H minerals, mainly Al-Foshagite, in this system, serve as precursors for the generation of γ-Al_2O_3 upon carbonation, mitigating the deterioration of photocatalytic properties. The findings are expected to provide new insights for the development and engineering practice of functional cementitious materials for durable cooling applications.

1. Introduction

1.1. Research background

In recent decades, radiative cooling technologies have gained global attention and have been extensively studied thanks to their significant potential for energy-free cooling and potential contributions to carbon neutrality [1]. Radiative cooling relies on both a high solar spectral reflectance (R_{sun}, λ∼0.3–2.5 μm) and a high atmospheric window spectral emissivity (ε_{aw}, λ∼8–13 μm) to maximize thermal dissipation through the long-wave infrared atmospheric transparent window to the universe and minimize solar energy gain [2].

Concerns have also been raised regarding the sustainability and durability of commercially developed organic radiative coolers [3–5]. The fabrication of organic radiative coolers often involves the use of toxic volatile solvents like tetrahydrofuran and dimethylformamide [6,7], and the release of volatile organic compounds (VOCs) during their service can pose health risks [4]. Moreover, the weak ultraviolet (UV) resistance of polymeric materials limits their applicability due to the degradation under long-term solar irradiation [8].

To address the aforementioned issues, inorganic radiative coolers for building applications have also been developed [1,9–11]. Among these, autoclaved cementitious pastes have been found to significantly increase R_{sun} and radiative cooling performance by promoting microstructural and phase composition alterations of the cementitious matrices [1]. Cementitious cooling pastes are manufactured using white cement, silica, alumina, and whitening agents under autoclave conditions. The main hydration products are amorphous and crystalline C–S–H phases. The types and contents of crystals in the generated C–S–H are determined by the properties and content of silica sources [12]. Additionally, the addition of aluminum sources (alumina and aluminum-bearing SCMs) under autoclave conditions can lead to the formation of aluminum-substituted C–S–H (C-A-S-H) and aluminum-based minerals (e.g., hydrogarnets) in cementitious systems [13,14]. The Mie resonances between the incident solar irradiation and the nano- and micro-hydrate particles promote Mie scattering on the cooler surface, which could further increase R_{sun}.

Additionally, by incorporating TiO_2 nanoparticles into cementitious matrixes, the photocatalytic self-cleaning mechanism driven by the UV band of solar irradiation has been empowered [14,15]. It is expected to resist the contamination of a cooler surface during service, thereby achieving durable and efficient radiative cooling. The contribution of

* Corresponding author. School of Civil Engineering, Wuhan University, Wuhan 430072, China.
E-mail address: q.yu@bwk.tue.nl (Q. Yu).

https://doi.org/10.1016/j.cemconcomp.2024.105626
Received 15 February 2024; Received in revised form 4 May 2024; Accepted 8 June 2024
Available online 10 June 2024

aluminum incorporation to the photocatalytic properties of cementitious materials has been revealed in previous studies [14,16]. However, (alumino-)silicate cement pastes, as a kind of cement-based material, would undergo carbonation when exposed to the ambient environment for long-term service [17,18]. The impact of carbonation on autoclaved cement pastes with silica addition could be magnified due to its higher amount of calcium silicate hydrate (C–S–H) phases than normal cement-based materials [1,19]. Changes in microstructure and phase composition driven by carbonation could consequently impact their optical properties for photocatalytic self-cleaning and radiative cooling [1,20,21].

Previous research has demonstrated that the carbonation behavior (kinetics and products) of C–S–H is influenced by the Ca/Si ratio, metal incorporation (e.g. the substitution of Si atoms in C–S–H by Al atoms), and existing phases [22–25]. The Ca/Si ratios of C–S–H were found to affect the decalcification process, and the presence of quartz has been shown to induce the generation of vaterite rather than calcite during carbonation curing [1,15,26,27]. The aluminum incorporation in C–S–H could also alter its carbonation kinetics [22,28]. Hence, it is reasonable to assume that the silica crystallinity (source), Ca/Si ratio, and alumina addition could impact the carbonation kinetics and products [14]. Consequently, the radiative cooling and photocatalytic self-cleaning performance of aluminosilicate cement pastes are affected [15,26].

Furthermore, autoclaved aluminosilicate cement pastes may exhibit different carbonation kinetics due to their distinct phase composition compared to normal cementitious systems [14,22,24,29,30]. Research investigating the effects of carbonation on the radiative cooling and photocatalytic self-cleaning properties of aluminosilicate cement pastes, as well as the influencing factors mentioned above, has not been reported. Therefore, studying the carbonation behaviors of aluminosilicate cement pastes and their impact on the physical and chemical properties is crucial for understanding the durability and engineering potential of multifunctional cementitious materials.

1.2. Scientific significance

Given the importance of an efficient self-cleaning mechanism for long-term efficient radiative cooling and the inevitable carbonation during service, this study aims to reveal the evolution of photocatalytic self-cleaning and radiative cooling properties of aluminosilicate cementitious pastes, with different physicochemical properties, upon carbonation. Specifically, the roles of silica (content and source), alumina, and the combination of silica and alumina on the carbonation durability of functionalities of multifunctional cementitious materials will be systematically investigated.

To achieve these goals, photocatalytic cement pastes are prepared with varying silica contents and sources, with and without alumina addition under autoclave conditions. The phase composition, microstructure, optical properties, and photocatalytic self-cleaning performance of the prepared pastes are characterized and analyzed using multiple techniques. On-site outdoor measurements are conducted to validate the cooling performance of the materials.

2. Materials and methods

2.1. Materials and sample fabrication

White Portland cement (CEM I 52,5 R, Aalborg White, 76 wt% C_3S, 16 wt% C_2S, 5 wt% C_3A, 1 wt% C_4AF), micro quartz powder (SF500, SIKRON, $d_{50} = 5$ μm), nanosilica (>99 %, EuroSupport), α-alumina (>99 %, Sigma Aldrich), and anatase titania (>99 %, Sigma Aldrich) are used for sample preparation. Contents of quartz, nanosilica, and alumina are adjusted to modify the C–S–H properties (Ca/Si ratio and aluminum incorporation) of the final products (Table 1). The photocatalyst is kept at 5 wt% of all mixes. XRD patterns and crystallinity of quartz and nanosilica can be found in our previous study [14]. The water-to-powder ratio (W/P) of 0.4 is used for all recipes, while the polycarboxylate-based liquid superplasticizer (SP, ViscoFlow-3000, Sika) is applied to ensure workability when nanosilica is used. To better observe and understand the impact of original cement chemistry on the radiative cooling and self-cleaning properties of aluminosilicate cement pastes, additional whitening agents (rutile TiO_2, calcite, and $BaSO_4$) are not used in this study.

Due to the varying particle size ranges of raw materials, different analytical devices are utilized. The particle size distributions (PSD) of cement, quartz powder, and alumina are determined using Mastersizer 2000 (Malvern), while the PSD of nanosilica and TiO_2 nanoparticles is determined using Zetasizer Nano (Malvern). The results are presented in Fig. 1.

Before sample preparation, the pre-mixing (200 rpm, 2 min) of dry powders is conducted using a planetary ball mill (Pulverisette 5, Fritsch) for better homogeneity. SP dispersions are prepared by mixing SP with 25 wt% deionized (DI) water with a magnetic stirrer for 30 s. Milled powder mixtures are first mixed with 75 wt% DI water at low speed for 60 s with a high-speed mixer (KitchenAid). The SP dispersion is then added to the bowl, mixed at low speed for 60 s, and then at high speed for 60 s. After mixing, paste slurries are cast into molds ($4 \times 4 \times 16$ cm^3), covered by plastic foils to prevent moisture loss and CO_2 exposure, and then cured at 20 ± 0.5 °C for 24 h. The hardened specimens are then demolded and cured under hydrothermal conditions (~13 atm, ~190 °C, ~8 h). After autoclave, specimens are cut into slices ($4 \times 4 \times 1$ cm^3). Some slices are dried in a vacuum chamber at 40 °C for 24 h for the characterization of uncarbonated samples. Other slices are saturated in DI water for 24 h to eliminate the impact of internal moisture and then moved to the climate chamber for accelerated carbonation.

In this study, a constant CO_2 concentration of 3 % is maintained throughout the carbonation process, the temperature is kept constant at 20 °C, the relative humidity is kept at 60 %, and a total duration of 14 d is applied.

2.2. Methodology

2.2.1. Phase composition

To characterize the phase composition of as-prepared aluminosilicate cement pastes, crushed paste pieces are milled using an XRD mill (McCrone, Retsch) and subsequently sieved to obtain particles below 40 μm in size. The mineral composition of aluminosilicate cement pastes is

Table 1
Mix design of cooling aluminosilicate cement pastes.

Sample	Materials [wt.%]					W/P	SP/P [%]
	Cement	Quartz	Nanosilica	Alumina	Titania		
A1	95	/	/	/	5	0.4	/
A2	76	19	/	/	5	0.4	/
A3	57	38	/	/	5	0.4	/
A4	57	19	/	19	5	0.4	0.7
A5	76	/	19	/	5	0.4	2.7
A6	57	/	19	19	5	0.4	4.1

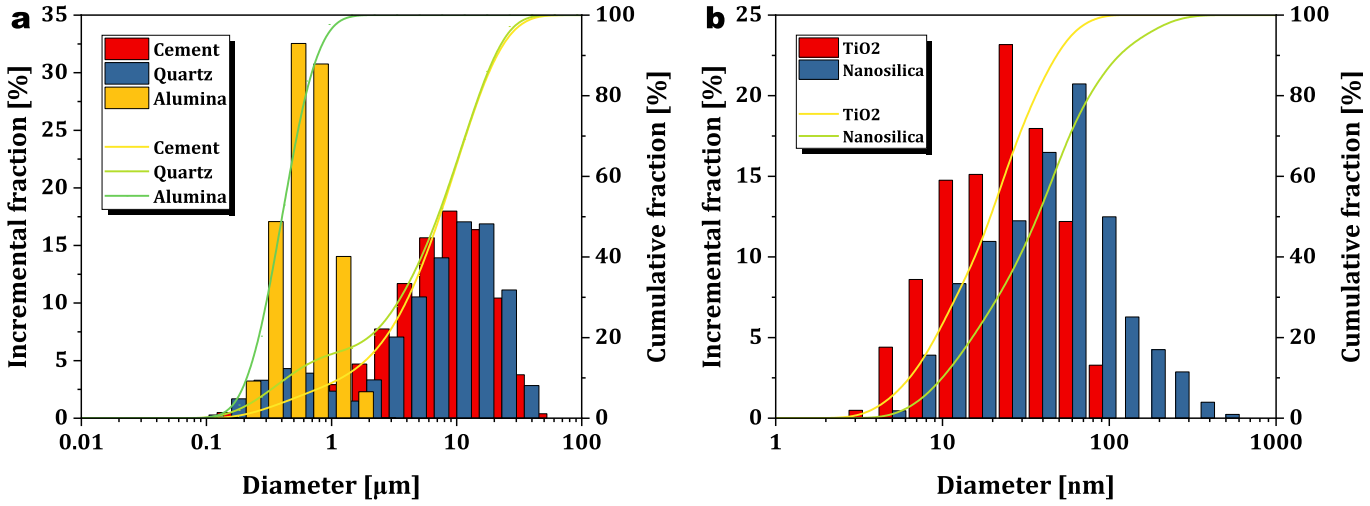

Fig. 1. Particle size distribution of raw materials.

determined using an XRD instrument (D4, Bruker), performed with a cobalt tube ($K\alpha_1$ of 1.78897 and $K\alpha_2$ of 1.79285), an accelerating voltage of 40 kV (15 mA), an interval of 0.02°/s, a residence time of 0.5 s, and the 2θ range set from 10 to 90°. Thermogravimetric analysis is conducted using a TGA device (STA 449 F1 Jupiter, Netzsch). Approximately 50 mg of each sample, in the form of ground fine powders, is heated from 40 to 1000 °C at a heating rate of 5 °C/min, with nitrogen used as the protective gas. The chemical bonds present in the samples are analyzed using an FTIR spectroscopy system (Frontier, PerkinElmer) equipped with an attenuated total reflection (ATR) crystal (GladiATR, PIKE technologies). The scanning range covered from 400 cm^{-1}–4000 cm^{-1} with a resolution of 1 cm^{-1}, enabling the identification of specific chemical functional groups.

2.2.2. Microstructure

Crushed species are sieved (3–4 mm) for MIP measurements. The Mercury porosimeter (AutoPore V, Micromeritics), working with a pressure between 14 kPa and 228 MPa, the surface tension of mercury of 485 N/m, and a contact angle of 130°, is applied in this study.

The fine paste particles sieved below 40 μm are dried and degassed at 40 °C under N_2 flow for 4 h. Subsequently, the processed powders are analyzed using a porosimeter (TriStar II 3020, Micromeritics) to determine the Brunauer-Emmet-Teller (BET) specific surface area (SSA) at −196 °C under an N_2 environment.

For SEM analysis, crushed thin pieces are put on holders and then coated with a thin layer of gold using a sputter coater (K550X, Emitech). The sputter coater applied a current of 30 mA for 30 s, resulting in the deposition of a conductive gold layer on the surface. The observation is conducted using microscopy (Phenom ProX, Thermo Fisher Scientific) operating at an accelerating voltage of 15 kV. The coupled energy-dispersive spectrometer (EDS) is utilized for quantitative analysis. It is noted that EDS analysis is typically applied to flat surfaces, particularly for the element mapping of a large area, because rough surfaces can cause a shadowing effect that may affect the accuracy of the analysis. in this study, However, the phases investigated by EDS are both crystals with clear morphologies and edges in SEM. Hence, the shadowing effect is not a concern in this situation when the spectrum acquisition for different spots is applied on these crystals.

2.2.3. Optical properties

Solar reflection spectra are measured using a UV-VIS-NIR spectrophotometer (UV-3102 PC, Shimadzu) equipped with an integrating sphere model (MPC-3100, Shimadzu). The spectra are recorded within the wavelength range of 300–2500 nm, with a scanning interval of 1 nm. Mid-infrared emissivity spectra (λ∼8–13 μm) are obtained using an FTIR spectroscopy (Frontier, PerkinElmer) equipped with an integrating sphere (IntegratIR, PIKE technologies). The spectra are recorded within the wavenumber range of 4000 cm^{-1} to 560 cm^{-1}, with a resolution of 1 cm^{-1}. The calculation of solar spectral reflectivity (R_{sun}) and atmospheric window spectral emissivity (ε_{aw}) follows:

$$R_{sun} = \frac{\int_{0.28\ \mu m}^{2.5\ \mu m} I(\lambda)R(\lambda)d\lambda}{\int_{0.28\ \mu m}^{2.5\ \mu m} I(\lambda)d\lambda} \quad \text{Eq. 1}$$

$$\varepsilon_{aw} = \frac{\int_{8\ \mu m}^{13\ \mu m} \sigma(\lambda)I_B(\lambda,T)d\lambda}{\int_{8\ \mu m}^{13\ \mu m} I_B(\lambda,T)d\lambda} \quad \text{Eq. 2}$$

$$I_B(\lambda,T) = \frac{C_1}{\lambda^5\left(e^{\frac{C_2}{\lambda T}}-1\right)} \quad \text{Eq. 3}$$

Where λ is the wavelength [nm], $R(\lambda)$ is the reflectance spectrum, $I(\lambda)$ is the global solar intensity spectrum at sea level from Ref. [31], $\sigma(\lambda)$ is the absorptivity spectrum, $I_B(\lambda,T)$ is the thermal emission spectrum of the blackbody at temperature T, C_1 is 3.743 × 10^{-16} W m^2, C_2 is 1.4387 × 10^{-2} m K.

Furthermore, the optical band energy is determined using Tauc plot, which is a general method of determining the optical band gap in semiconductors, by applying the absorption spectra over the UV-VIS range [32].

2.2.4. Photocatalytic self-cleaning performance

To avoid the impact of moisture level on photocatalytic properties, polished slices are saturated with DI water by immersing them for 24 h and then naturally dried overnight (20 ± 1 °C), and then stained by Rhodamine b (RB) solution (0.1 mM), and then naturally dried in a black box overnight (20 ± 1 °C) [33]. Stained slices are irradiated by a UV lamp (10 W/m^2) the wavelength ranges from 300 nm to 400 nm, centered at 345 nm, at 0 min, 10 min, 30 min, 120 min, 600 min, and 2400 min. And then the surfaces are scanned by a UV-VIS spectrometer (USB 4000, Ocean optics) equipped with a halogen light source (HL-2000-FHSA, Ocean Optics). CIE a*, which is the dominant coordinate of dye RB in the CIE Lab color space, is collected with 60 scans after each radiation time of each slice, and the average is used [30]. The discoloration rates/self-cleaning performance (φ_t) at different irradiation times are calculated by:

$$\varphi_t = \frac{a_0 - a_t}{a_0} \times 100\ \% \quad \text{Eq. 4}$$

Where a_0 is the a* before UV irradiation and a_t is the a* after t min UV irradiation.

2.2.5. On-site cooling performance measurement

The field measurements are conducted on the SolarBEAT Roof at the Vertigo Building (51.44641°N, 5.48511°E), TU Einhoven (https://www.tue.nl/en/research/research-labs/solarbeat/). The cooling performance of aluminosilicate cement paste slices (4 × 4 × 1 cm^3) is determined by the experimental setup as depicted in Fig. 2. The measurement setup consists of the following components:

1. Insulation boxes: Three insulation boxes, each with dimensions of 10 × 10 × 10 cm^3, are utilized. These boxes are constructed with a steel base and aluminum foil, along with three insulation layers. Each insulation layer had a thickness of 2 cm. The thermal conductivities of the extruded polystyrene (XPS, JACKODUR Plus 300 Standard, Jackson insulation) layer and silica aerogel (IC3100, Cabot) layers are 0.027 W/(m·K) and 0.012 W/(m·K), respectively. The insulation layers and reflective foil are employed to minimize the thermal gain of boxes, while the steel base ensures stability.
2. Pyranometer and sun tracker: A pyranometer (MS802, EKO Instruments) is used to measure solar radiation, while a sun tracker (STR220, EKO Instruments) is employed to precisely track the movement of the sun.
3. Wind sensor: A wind sensor (V200A Ultrasonic, Lufft) is utilized to measure wind speed.
4. Thermistor sensors: Three high-accuracy thermistor sensors (NTC, SENSOR DATA, ±0.05 °C) are employed to measure the internal temperature.
5. Data logger: A data logger model SQ2040 (Grant) is used to collect and record the data from the various sensors.

All the data are collected with an interval of 1 min. To prevent heat convection between the air and the cooling slice, a transparent polyethylene (PE) film is placed above the cooling slice, maintaining a 0.5 cm gap. An infrared camera (B360, FLIR) is used to capture thermal images. It is important to note that the default emissivity of 0.9, distance of 1.0 m, and air temperature of 25.0 °C are utilized for surface temperature measurements. Obtained IR photos are processed by the assembled software (ThermaCAM Researcher Professional 2.8 SR-1) for background and area temperature acquisition.

Furthermore, it should be noted that all measured temperatures, both surface and internal, of the cooling slices installed on the insulation boxes are intended to demonstrate the cooling performance of the prepared materials. Further field studies are necessary to assess the actual performance of these materials in real engineering practice.

3. Results

3.1. Crack formation upon autoclave curing and accelerated carbonation

Crack formation is a major failure pattern for cementitious materials [34]. In this study, visible cracks are observed in some samples upon the hydrothermal hydration and accelerated carbonation (Fig. 3). After the autoclave treatment, A5 with a high volume of nanosilica addition (19 wt%), presents structural failure and breaks into two parts with a typical expansion cracking. Meanwhile, no cracks are observed in A6, although A6 is also prepared with 19 wt% of nanosilica and an additional 19 wt% of α-alumina. These results demonstrate that the use of α-alumina could prevent the crack formation of aluminosilicate cement pastes upon autoclave curing, when the high-volume nanosilica is used.

Following the accelerated carbonation, cracks in carbonated A2 make the slice fragile which could not keep the structural integrality, while visible cracks are observed in A3 but with a good structural integrality. These results demonstrate that the increase in quartz content does not always promote the formation of cracks upon carbonation. Unreactive fillers could also play an important role in preventing crack formation, as no cracks were observed in our previous study when unreactive whitening agents were used upon autoclave and accelerated carbonation [1]. Hence, more of the unreactive quartz works as fillers in A3.

According to the results above, silica source and alumina addition significantly affect the cracking behavior upon hydrothermal hydration and accelerated carbonation. As a result, the discussion of radiative cooling and photocatalytic self-cleaning properties in this study will focus on samples A1, A4, and A6, where cracks are not observed. The

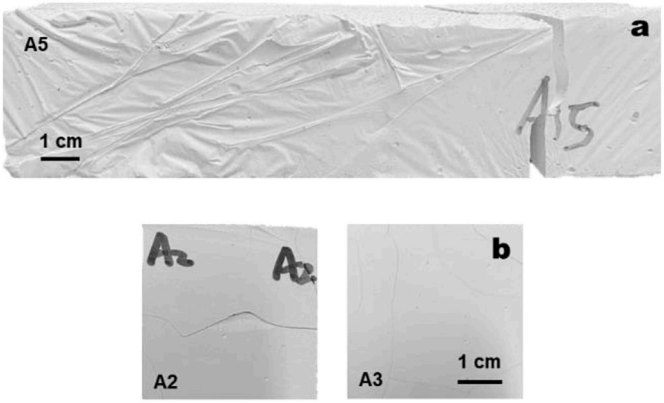

Fig. 3. (a) Sample A5 with cracks upon autoclave curing and (b) Samples A2 and A3 with cracks upon carbonation.

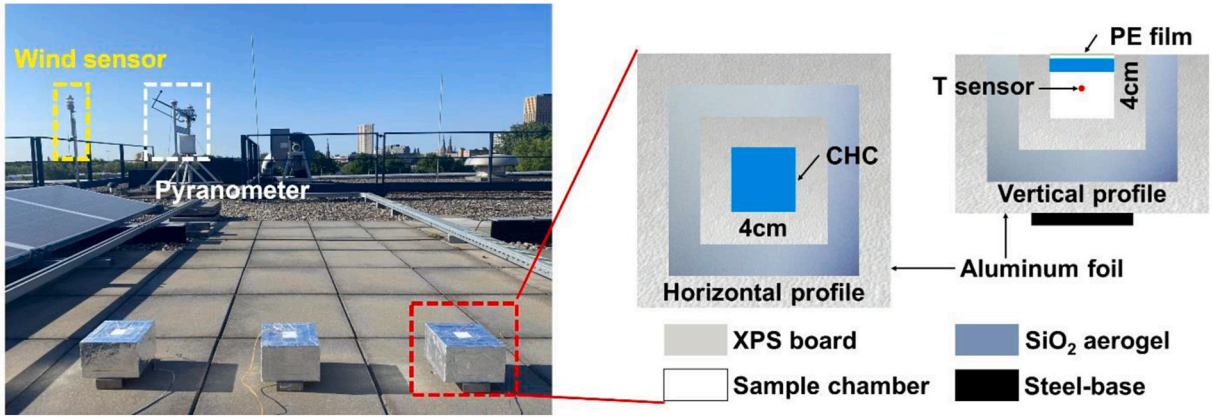

Fig. 2. Schematic of the on-site cooling performance measurement setup.

mechanism of crack formation, concerning the silica source, hydration kinetics, carbonation kinetics, and aluminum incorporation, will be also discussed in the subsequent sections, considering the phase composition and microstructure evolution upon autoclave treatment and accelerated carbonation.

3.2. Phase composition

3.2.1. Phase composition before carbonation

Fig. 4 presents the XRD patterns of uncarbonated aluminosilicate cement pastes, revealing the crystalline phase composition. The peaks located around 2θ = 21.059° and 2θ = 39.895° are indications of the presence of calcium hydroxide (portlandite), and they are predominantly intense in sample A1. The peaks of portlandite are diminished in other samples due to the high-temperature pozzolanic reactions following the addition of reactive oxides (nanosilica, quartz, and alumina). This is in line with the thermogravimetric results as the content of portlandite in sample A1 is much higher than in other samples. Another significant observation is the peak at around 2θ = 29.494°, attributed to anatase TiO_2, which is a consequence of the incorporation of the photocatalyst. Additionally, quartz (2θ = 31.017°) is detected in samples A2, A3, and A4, with varying peak intensities (A4 > A3 > A2). The results indicate that, under autoclave conditions, $Ca(OH)_2$ preferentially reacts with alumina rather than quartz and alumina can stoichiometrically bind more calcium than quartz. Hydrogarnet minerals, including katoite (2θ = 20.388°/37.705°/46.626°), and hibschite (2θ = 20.737°/38.367°/47.463°), are identified in samples A1 and A4. The close diffraction angles of katoite and hibschite are attributed to similar crystal structures. The peak intensities of hydrogarnets in sample A4 are much higher than in sample A1, which is attributed to the different aluminum availability. The aluminum may originate from aluminum-bearing clinkers (1.63 wt% Al_2O_3 of unhydrated cement) as well as additional alumina.

Furthermore, crystalline C–S–H (2θ = 34.225°/37.400°) and various C–S–H minerals, including jaffeite (2θ = 35.957°/36.798°), tobermorite11 Å (2θ = 33.767°/34.936°), jennite (2θ = 34.225°/35.677°), tobermorite 14 Å (2θ = 33.812°/34.683°), and foshagite (2θ = 35.265°), have been identified across different samples. The close diffraction angles (2θ = 32.5°–37.5°) of these C–S–H phases are also attributed to their similar crystal structures.

The presence of C–S–H phases across different samples is included in Table S1. In sample A1, the presence of jaffeite, crystalline C–S–H, and tobermorite 11 Å are observed. Sample A2 exhibits tobermorite 14 Å, tobermorite 11 Å, and jennite. In sample A3, tobermorite 11 Å and tobermorite 14 Å are observed. The dominant C–S–H mineral changes from jaffeite (A1) to tobermorite 14 Å (A2), and then to tobermorite 11 Å (A3), in tandem with the $CaO:SiO_2$ stoichiometric ratio varying from 4:1 to 1.6:1, and then to 0.9:1, when cement is replaced by quartz. This discrepancy could be attributed to the average coordination number of water molecules available to the Si–O tetrahedron, according to the different $SiO_2:H_2O$ stoichiometric ratios of these C–S–H minerals as shown in Table S1. With the co-use of quartz and alumina, crystalline C–S–H and jaffeite are observed in sample A4. Samples A5 and A6 exhibit similar patterns, with the presence of foshagite and crystalline C–S–H. Tobermorite 11 Å is observed in sample A6, but tobermorite 14 Å in sample A5, which is also in line with the discussion on H_2O availability above, concerning the Basal spacing of tobermorite crystals [35]. Meanwhile, alumina and other aluminum-bearing phases are not detected by XRD, which indicates that aluminum is completely incorporated into the C–S–H phases, with the generation of C-A-S-H phases (amorphous + crystalline).

The TGA and DTG results, as depicted in Fig. 5 and detailed in Table S1, offer insights into the phase composition and thermal decomposition behavior of different samples. Amorphous C–S–H gel exhibits gradual mass loss due to the release of loosely bound and interlayer water, occurring over a broad temperature range from 40 °C to 200 °C. Under autoclave conditions, the crystallinity of C–S–H could be slightly increased [1,14]. Hence, the poor-crystalline C–S–H necessitates an additional depolymerization process, resulting in a higher decomposition temperature of 320 °C [36]. The incorporation of aluminum causes amorphous C-A-S-H gel to decompose at higher temperatures compared to C–S–H, within the range of 40 °C–600 °C [35].

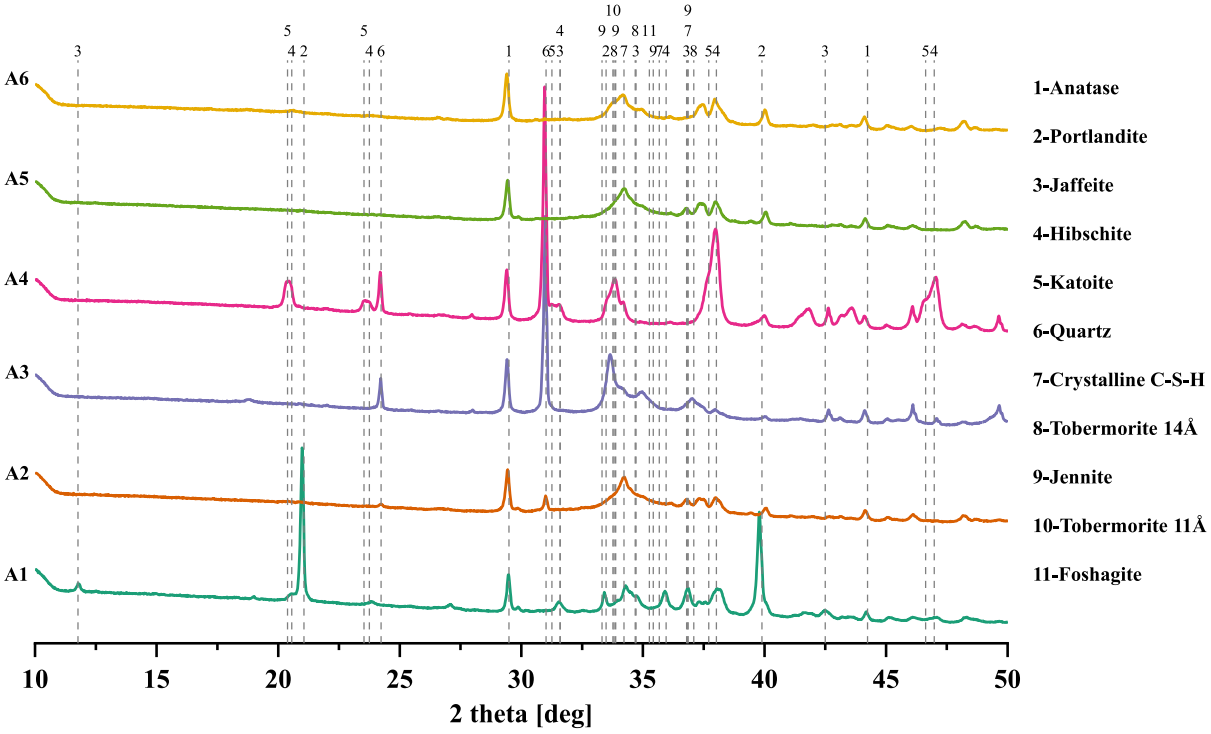

Fig. 4. X-ray diffraction patterns of uncarbonated aluminosilicate cement pastes.

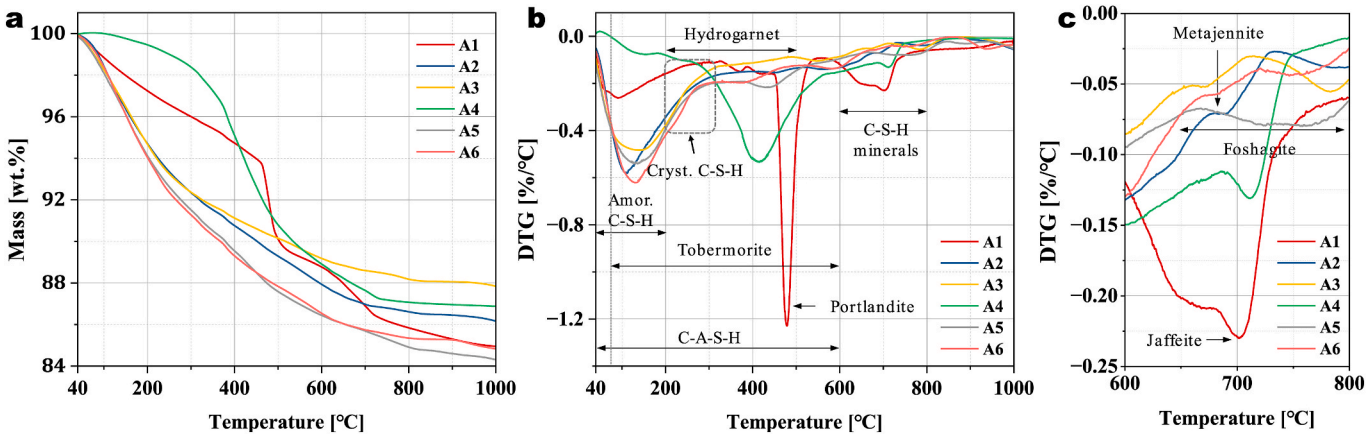

Fig. 5. TGA-DTG curves of uncarbonated aluminosilicate cement pastes.

The mass loss observed between 450 °C and 550 °C can be attributed to the dehydroxylation of portlandite, with sample A1 displaying more pronounced mass loss in this range compared to other samples. The thermal decomposition of C–S–H minerals may involve two distinct steps, commencing with dehydration at lower temperatures and followed by dehydroxylation at higher temperatures [36]. Dehydration temperatures may vary in different literature sources. For example, the dehydration temperature from jennite to the metastable phase (metajennite) was described as 100–250 °C in one literature [36] and 70–90 °C in another [37]. Tobermorite phases exhibit mass loss beginning at 80 °C and extending up to 600 °C. As the temperature increases, the crystal structure of tobermorite changes, marked by the gradual loss of interlayer water molecules and a decrease in Basel spacing. The thermal decomposition temperatures for other phases are as follows: jaffeite at 550–800 °C and foshagite at 650–800 °C [38–40]. Different decomposition temperature ranges of hydrogarnets have been reported in various studies [41,42]. Based on the DTG curves as shown in Figs. 5 and 7, hydrogarnets in this study could decompose between 200 and 500 °C.

With the addition of α-alumina and different silica sources, different phase compositions are observed, especially the different C–S–H phases. Different phase compositions are expected to further affect optical properties for radiative cooling and carbonation behaviors. Discussions will be given in the subsequent sections.

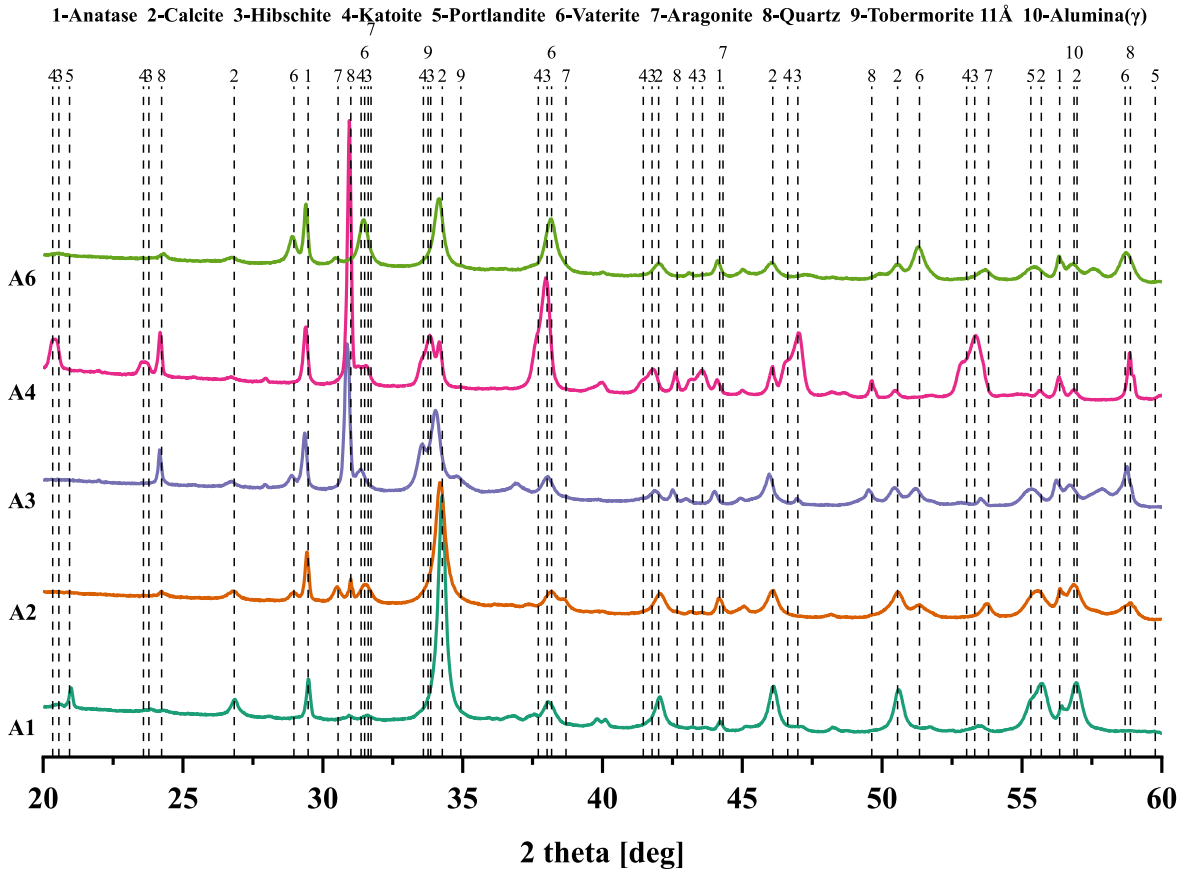

Fig. 6. X-ray diffraction patterns of carbonated aluminosilicate cement pastes.

3.2.2. Phase composition after carbonation

The X-ray diffraction patterns of samples subjected to carbonation are depicted in Fig. 6. Distinct polymorphs of calcium carbonates are observed in different samples. Calcite is present in all samples except for sample A3. Among these samples, sample A1 exhibits the highest diffraction intensity of calcite, emphasizing the role of portlandite in calcite formation, as the direct precursor. Additionally, two other polymorphs, vaterite, and aragonite, are observed in all samples. Most C–S–H mineral phases, except for tobermorite 11 Å, display disappearing peaks in all samples, indicating the different carbonation kinetics of different C–S–H minerals. Tobermorite 11 Å is observed in all samples, except for sample A4, which demonstrates the higher carbonation resistance of tobermorite 11 Å than other C–S–H phases. Hydrogarnets are deemed stable under accelerated carbonation (3 % CO_2), a conclusion supported by both XRD and TGA results. Intriguingly, a new phase, gamma-alumina (γ-Al_2O_3), in carbonated sample A6 is detected with the XRD analytical software (HighScore Plus). However, the strong overlap of diffraction peaks of calcite and γ-Al_2O_3 renders this evidence weak. Nevertheless, SEM and EDS observations, as depicted in Fig. 11e, confirm the presence of gamma-alumina in carbonated sample A6.

According to TGA and DTG results, the different polymorphs of calcium carbonates are determined by decomposition temperatures (Fig. 7). The mass loss between 730 °C and 850 °C is assigned to calcite. Aragonite and vaterite, as the metastable calcium carbonate minerals, decompose at lower temperatures of 660–730 °C [43,44]. The decomposition temperature range of amorphous calcium carbonate is lower than the crystalline ones, which is determined as 400–660 °C. After carbonation, C–S–H is also observed in all samples, which is attributed to the existence of the critical Ca/Si ratio for the decalcification of C–S–H gel [44]. It is important to note that the overlapping decomposition temperatures (400–500 °C) of hydrogarnet and amorphous calcium carbonate can affect the temperature-based mass calculations. Therefore, sample A4 is excluded from the mass calculation.

The contents of distinct calcium carbonate phases are presented in Table 2. Among these phases, amorphous calcium carbonate emerges as the dominant calcium carbonate phase, with the content ranking as follows: A2 > A3 > A1 > A6. This finding diverges from observations on general OPC-based materials, where calcite typically dominates as the major calcium carbonate polymorph. This discrepancy could be attributed to the increased contents of C–S–H phases in autoclaved cement-based materials (with silica) [1]. The content of vaterite/aragonite in samples A1, A2, and A6 is similar and higher than in sample A3. Concerning calcite, sample A1 exhibits a significantly higher content compared to samples A2 and A6, while sample A3 displays a notably low calcite content of approximately 0.80 wt%.

In addition to microstructural refinement, the generated carbonation products could also precipitate on the surface of TiO_2 nanoparticles, resulting in a sheltering effect and the occupation of active sites, which may influence the photocatalytic properties [45]. Additionally, crystalline calcium carbonates may exert a stronger impact due to their denser microstructure compared to the amorphous forms [15].

Table 2
Contents of calcium carbonates based on TGA-DTG results.

Sample	Content [wt.%]			
	$CaCO_3$ (amor)	Vaterite/Aragonite	Calcite	Cumulative
A1	21.59	9.61	19.70	50.91
A2	30.57	10.27	5.18	46.02
A3	24.91	4.93	0.80	30.64
A6	21.59	10.64	4.93	37.16

In addition to the conventional carbonation kinetics observed in C–S–H phases, the results presented in **Section 3.2.1** and **Section 3.2.2** may reveal one distinct carbonation kinetic for Al-foshagite. This particular kinetic appears to be a novel finding and has not been previously reported. By tracing the element aluminum, γ-Al_2O_3 could potentially originate from aluminum-bearing phases, including amorphous C-A-S-H, crystalline C-A-S-H, and Al-foshagite. The incorporation of aluminum in crystalline C–S–H and foshagite has been determined by EDS analysis, as shown in Fig. S1. However, previous studies on the carbonation of amorphous and poorly crystalline C-A-S-H in cement-based and geopolymer-based systems have not identified γ-Al_2O_3 as a carbonation product [46,47].

It can therefore be inferred that high-crystalline C-A-S-H minerals, mainly Al-Foshagite, with a relatively higher Al/Si molar ratio, generated under autoclave conditions, serve as the aluminum source for γ-Al_2O_3 generation upon carbonation. This suggests that Al-Foshagite is the major precursor responsible for the generation of γ-Al_2O_3 upon carbonation. This transformation from α-Al_2O_3 to γ-Al_2O_3, facilitated by Al-Foshagite as an intermediate, is significant. Unlike α-Al_2O_3, γ-Al_2O_3 is known for its excellent adsorption and catalytic properties as a typical porous medium. Therefore, as a good catalytic support, the generated γ-Al_2O_3 may partially compensate for the degradation in photocatalytic performance caused by carbonation, a topic that will be discussed in the following sections.

Meanwhile, a limited decrease in SSA is observed with the generation of γ-Al_2O_3 (alongside the generation of silica gel) upon carbonation (Table S2). This indicates that γ-Al_2O_3 and silica gel are porous and can provide more active sites than other carbonation products.

3.3. Microstructure

In cementitious systems, pores are typically categorized as follows: 1) gel pores (GP) with diameters below 10 nm, 2) medium capillary

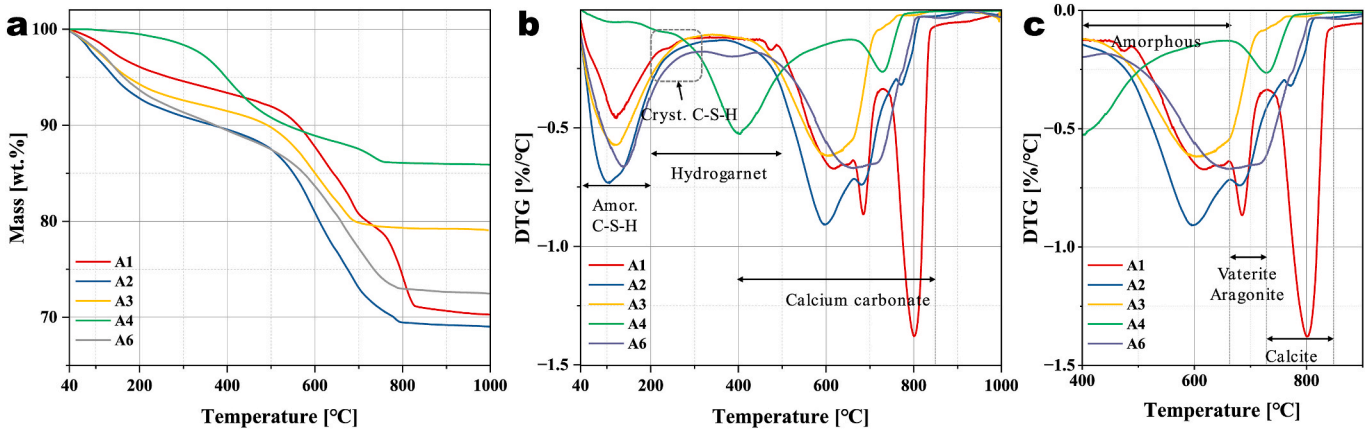

Fig. 7. TGA-DTG curves of carbonated aluminosilicate cement pastes.

pores (MCP) with diameters ranging from 10 nm to 50 nm, 3) large capillary pores (LCP) with diameters ranging from 50 nm to 1 μm, and 4) macropores (MP) with diameters exceeding 1 μm [15]. These categories are believed to make distinct contributions to the photocatalytic and radiative cooling properties of cementitious materials, based on fundamental principles in photocatalysis and radiative cooling [1,14].

3.3.1. Microstructure of aluminosilicate cement pastes before carbonation

Fig. 8 shows the cumulative and incremental pore size distributions of uncarbonated aluminosilicate cement pastes, while porosity and average pore diameter are presented in Table 3. With the addition of quartz addition (from A1 to A2), the microstructure is refined with a decreased porosity, average pore diameter, and LCP volume. Meanwhile, the same GP volumes are observed in samples A1 and A2, with a decrease in the volume of large capillary pores of sample A2. The hydrothermal pozzolanic reaction between quartz and alkali is considered to promote the generation of C–S–H phases, thus increasing the volume of gel pores. This anomaly could be attributed to the different contributions of the C–S–H phases to gel pore volume, as different dominant C–S–H minerals are observed in samples A1 and A2. With the further addition of quartz (from A2 to A3), the porosity slightly decreases however the average pore diameter decreases by 57.1 % (from 28.7 nm to 12.3 nm). The decrease in the volume of large capillary pores in samples A2 and A3 is attributed to the "filling" effect of unreactive quartz particles.

The microstructure of sample A4 is considerably coarsened with a porosity of about 42 % and an average pore diameter of above 100 nm with a great increase in large capillary pore volume. Similar results were observed in our previous study when a high volume of alumina was used with the generation of a high amount of hydrogarnet. With the substitution of cement by 18 wt% nanosilica, samples A5 and A6 present similar porosities and average pore diameters. The extra substitution of cement by alumina slightly increases the large capillary pore volume.

Fig. 9 displays different phases with varying morphologies in different samples before undergoing the carbonation process. It is noted that different magnifications were applied to better observe distinct phases and morphologies. Sample A1 exhibits distinct clusters of jaffeite and partially reacted portlandite. This suggests potential reactions for the production of jaffeite, possibly involving portlandite as a necessary precursor [48]. Samples A2 and A3 present different morphologies of tobermorite. Sample A2 showcases nanocrystal whiskers, while sample A3 displays microcrystal flakes. Nanosized whiskers, as seen in sample A2, are expected to provide more active sites for photocatalytic reactions. The morphologies of C–S–H minerals are not completely the same as reported in the previous study [14]. It demonstrates that the CaO/SiO_2 ratio of raw materials also affects the morphology of generated C–S–H minerals.

Sample A4 is profiled by hydrogarnet particles with a diameter of about 1 μm. Particles of this size can effectively scatter solar irradiation, which is a favorable property for radiative cooling [1]. Sample A5 features nano foshagite whiskers and cracks. The extension and growth of these microcracks lead to the structural failure of sample A5 upon the autoclave curing. The mechanism behind crack formation will be discussed further in **Section 4.1**. Sample A6 exhibits a honeycomb-like structure composed of Al-foshagite/crystalline C-A-S-H. This morphology is similar to that observed in synthesized semi-crystalline C-A-S-H [49]. Comparatively, the Al-foshagite honeycomb shows smaller pore diameters, indicating a potentially higher impact as a photocatalytic support. Additionally, the presence of pores with a diameter of about 1 μm is advantageous for scattering solar radiation [1]. The morphology of the C-A-S-H crystals observed in this study differs somewhat from that observed in previous studies, which may be attributed to variations in the Ca/Si ratios of the raw materials [50].

3.3.2. Microstructure of aluminosilicate cement pastes after carbonation

After carbonation, the expected refinement in porosity for all matrixes occurs (Table 3). The larger variation in porosity for A2 compared to A3 can explain the more pronounced cracking observed in sample A2 upon carbonation.

Upon carbonation, substantial decreases in surface area and medium capillary pores are observed in samples A1 and A4, while sample A6 retains approximately half of its medium capillary pores and about 80 % of its surface area as presented in Fig. 10 and Table S2. The reduction in medium capillary pores can significantly impact the photocatalytic properties of the aluminosilicate cement pastes, as these pores play a crucial role in the mass transport of photocatalytic reactions [15,26]. Additionally, the reduction in surface area could negatively affects the photocatalytic properties by lowering the amount of active sites to initiate photocatalytic reactions [49].

Fig. 11 presents SEM images of samples subjected to carbonated aluminosilicate cement pastes. Sample A1 displays a profile containing calcite (cubic), vaterite (packed particles), aragonite (fibrous), and amorphous phases (e.g. amorphous $CaCO_3$ and silica gel). In sample A2, both calcite and aragonite are observed. Sample A3 exhibits uncarbonated tobermorite 11 Å, with carbonation products (amorphous $CaCO_3$ and silica gel) precipitating on the edges of the tobermorite crystal flakes. This observation suggests that the carbonation of tobermorite 11 Å follows a dissolution-precipitation process. The relatively low solubility of tobermorite 11 Å may explain its high resistance to carbonation, as crystalline tobermorite 11 Å is less soluble than amorphous C–S–H gel [35,51]. Amorphous carbonation products precipitated on hydrogarnet particles are observed in sample A4. γ-Al_2O_3 crystals are observed in

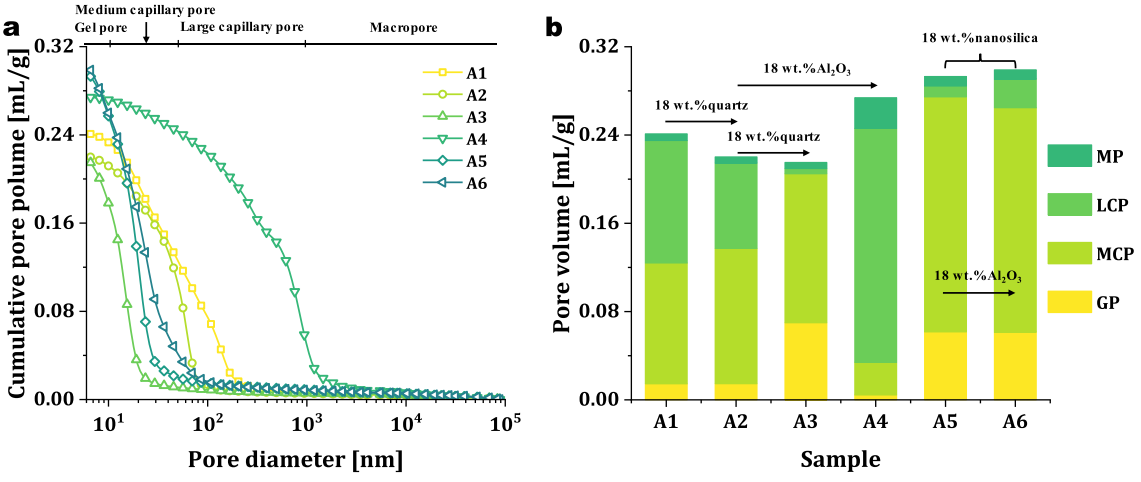

Fig. 8. (a) Cumulative pore size distribution and (b) Pore volumes of uncarbonated aluminosilicate cement pastes.

Table 3
MIP porosity, average pore diameter, and skeletal density of aluminosilicate cement pastes.

Sample	Porosity [%]		Average diameter [nm]		Skeletal Density [g/mL]	
	Uncarbonated	Carbonated	Uncarbonated	Carbonated	Uncarbonated	Carbonated
A1	36.4	16.4	31.1	60.2	2.37	2.22
A2	32.1	14.2	28.7	20.6	2.15	2.12
A3	31.6	23.2	12.3	18.9	2.15	2.21
A4	41.8	33.4	104.5	481.4	2.63	2.27
A5	38.4	/	14.9	/	2.12	/
A6	38.6	26.2	16.7	21.7	2.10	2.08

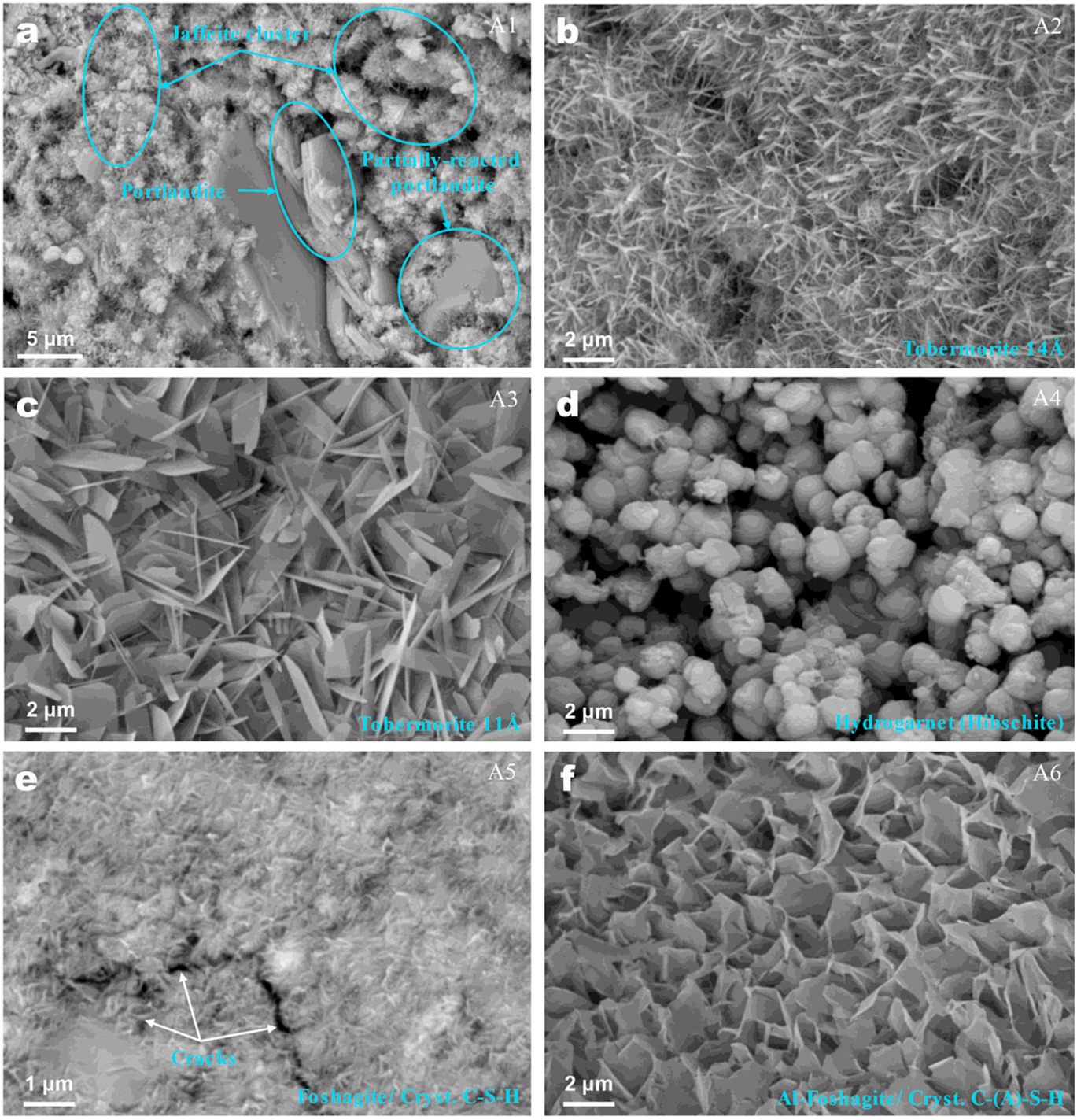

Fig. 9. SEM profiles of uncarbonated aluminosilicate cement pastes.

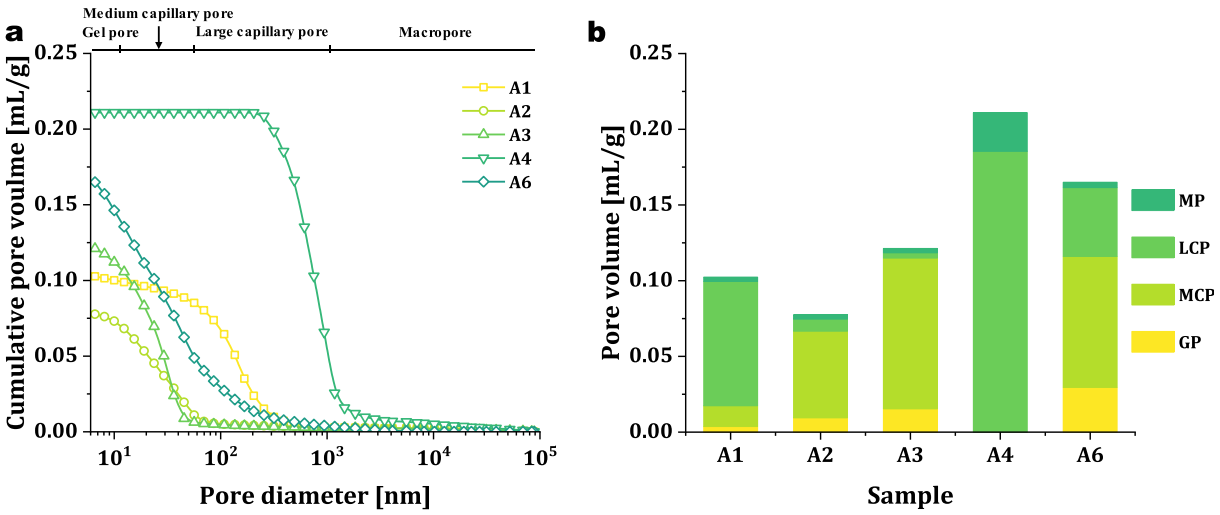

Fig. 10. (a) Cumulative pore size distribution and (b) Pore volumes of carbonated aluminosilicate cement pastes.

carbonated sample A6, which is aligned by the EDS element analysis (EDS spectrums are concluded in Fig. S2) and consistent with the XRD analysis.

The significant evolution of micromorphologies upon carbonation could alter the microstructural, micromechanical, and optical properties, especially for A2 and A6. The carbonation of jaffeite to calcite in A1 causes decreases in SSA and porosity, which contributes to the degradation of photocatalytic activity (Table 3 and Table S2). It demonstrates the two negative impacts induced by microstructural refinement: 1) the reduction of active sites available for photocatalytic reactions and 2) the limitation of micro mass transport. Compared to A3, A2 presents a more destructive microstructure with big calcite crystals (>2 μm) and massive microcracks, while A3 reserves partial microcrystals of tobermorite. Meanwhile, a higher content of calcite in A2 than in A3 is observed by TGA, as the generation of calcite holds higher solid volume expansion than other calcium carbonate polymorphs (Table 2) [17]. Hence, it is concluded the volume expansion caused by calcite generation could contribute to the different cracking patterns of A2 and A3.

Upon carbonation, the micro-sized honeycomb-like microstructure of C-A-S-H phases in A6 transforms into a profile consisting of amorphous gel and γ-Al_2O_3 crystals. The elimination of micro-sized honeycombs could reduce the Mie scattering capacity of A6, thereby contributing to the drop in R_{sun}. The refinement of the microstructure affects the mass transport for photocatalytic reactions, but the porous structure of amorphous gel and generated γ-Al_2O_3 can compensate for the loss in photocatalytic performance to some extent [28].

3.4. Optical properties

The optical properties of aluminosilicate cement pastes can affect both the photocatalytic self-cleaning and radiative cooling properties. The optical band gap energy can affect the photon utilization efficiency thus influencing the photocatalytic performance, where the radiative cooling power is determined by R_{sun} and ε_{aw} [42,67]. Samples A2 and A3 are excluded from the analysis of optical properties, thanks to the cracking upon carbonation.

3.4.1. Optical band gap energy

Fig. 12 presents the UV-VIS spectrums and Tacu's plots of aluminosilicate cement pastes A1, A4, and A6, with the band gap energies summarized in Table 4. These spectrums show different extents of variation upon carbonation, which could be mainly attributed to carbonation-induced phase changes. For sample A1, carbonation involves two major processes: (1) portlandite is almost completely carbonated to $CaCO_3$, and (2) decalcification of C–S–H phases to form amorphous C–S–H (with a low Ca/Si ratio), $CaCO_3$, and silica gel. In samples A4 and A6, the C-(A)-S-H phases are carbonated. Due to the existence of the critical Ca/Si ratio for C–S–H decalcification, C–S–H can not be entirely decomposed by carbonation [17]. Additionally, sample A4 contains significant amounts of carbonation-stable phases (hydrogarnet and unreacted quartz). Based on this analysis, the extent of variation in the spectrums should rank as A1 > A6 > A4. This ranking aligns with the observations in R_{sun} and ε_{aw} as shown in Figs. 12 and 13.

Band gap energy is considered an important parameter to predict the photocatalytic activity, however, the band gap energies of measured aluminosilicate cement pastes vary between a narrow range (3.03 eV (λ~409 nm) - 3.07 eV (λ~404 nm)) before and after carbonation in this study (Fig. 12 and Table 4). The results indicate the photocatalytic activities between aluminosilicate cement pastes in this study are less affected by the band gap energy, but more by phase composition and microstructure, which will be discussed further in the following sections.

3.4.2. Optical properties for radiative cooling

Carbonation has varying effects on the optical properties of the aluminosilicate cement pastes, with R_{sun} being more sensitive to carbonation compared to ε_{aw}, as depicted in Fig. 13. In general, carbonation leads to a decrease in R_{sun}. Specifically, R_{sun} decreases by approximately 2.5 % for sample A1, 0.5 % for sample A4, and 1.1 % for sample A6 (Table 5). In contrast, upon carbonation, ε_{aw} increases by roughly −2.0 % for sample A1, while the corresponding values for samples A4 and A6 are around 0.2 % and 0.4 %, respectively.

Before carbonation, sample A1 exhibits the best radiative cooling performance. However, it also displays the lowest durability against the deterioration of radiative cooling optical properties caused by carbonation. After carbonation, all samples show a R_{sun} of about 88.8 %, with the ε_{aw} of samples A4 and A6 exceeding that of A1 (92.8 % for A1, 94.0 % for A4, and higher for A6). Considering the slow carbonation speed in a real environment, sample A1 is still the best option in terms of radiative cooling. The superior durability of samples A4 and A6 against carbonation-induced changes in radiative cooling properties also suggests that they are good alternatives for long-term applications.

Meanwhile, cementitious coolers with R_{sun} and ε_{aw} both above 0.9 are prepared without the addition of whitening agents, as optical parameters of samples A1 and A6 ensure their high-performance radiative cooling, as presented in Fig. S4. This suggests that the whitening agent is not necessary for producing high-performance cementitious radiative coolers.

In previous studies, nano and micro pores and particles were

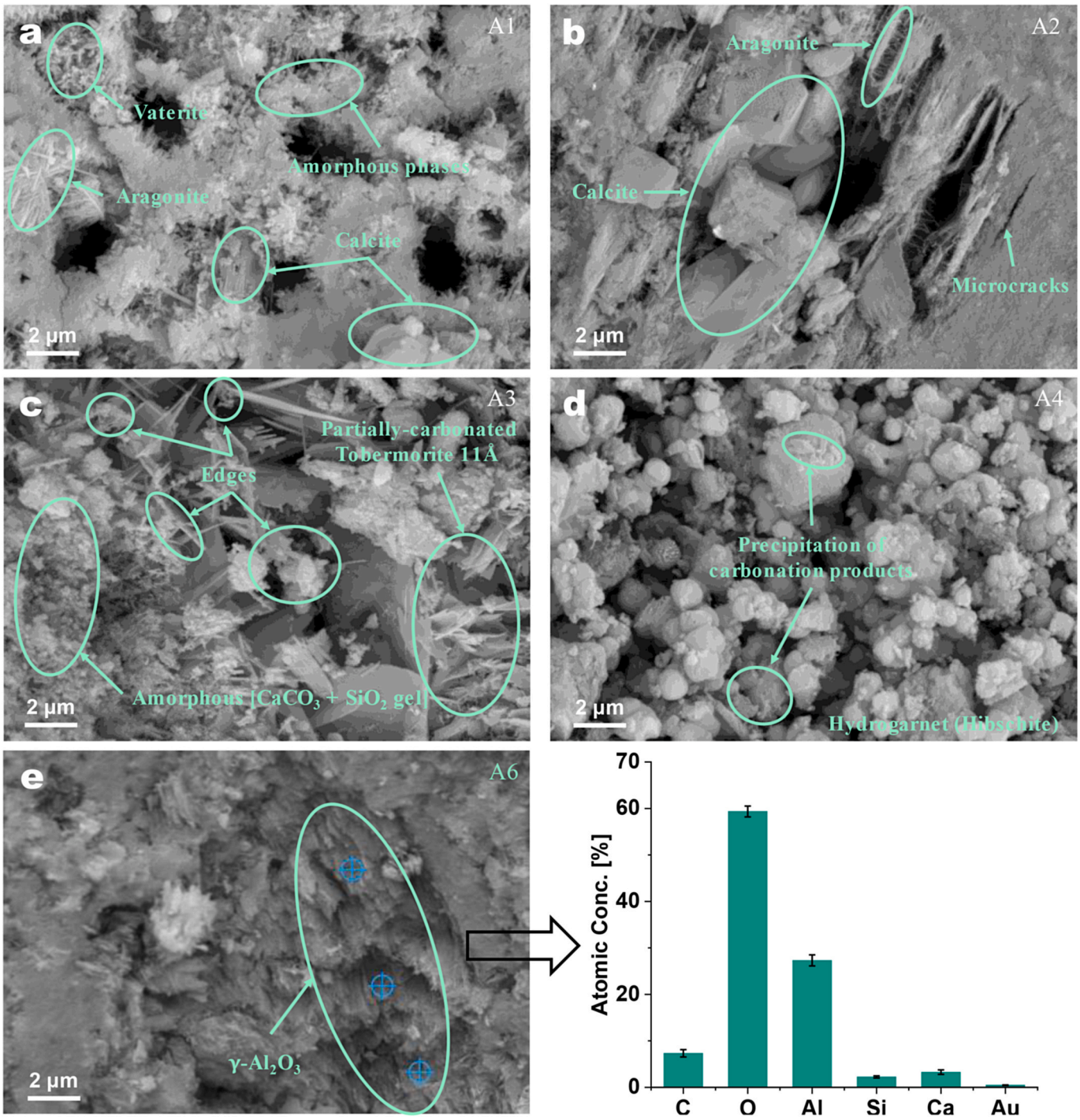

Fig. 11. (a–e) SEM images of aluminosilicate cement pastes carbonated and (f) Atomic concentration of elements of detected spots of γ-Al_2O_3.

considered to affect the optical properties for radiative cooling of cementitious radiative coolers, as well as other radiative coolers [1,52]. In this study, uncarbonated sample A4 (10^8/g-10^{12}/g) exhibits a higher amount of pores in the solar range compared to uncarbonated A1 and A6 (10^7/g-10^{12}/g) (Fig. S5 and Fig. S6). However, sample A4 shows the lowest R_{sun} among all tested samples (Table 5). This demonstrates that the pore number of uncarbonated samples has a limited impact on R_{sun} and ε_{aw}, likely due to their low and close magnitudes that cannot trigger effective Mie scattering [1]. After carbonation, the microstructure of all samples is considerably refined, and the differences of pore numbers between all samples are further narrowed (Table 3 and Fig. S6). The impact of pores on Mie scattering is further restricted.

3.5. Photocatalytic self-cleaning performance

The discoloration process of the samples exhibits different patterns before and after carbonation, as illustrated in Fig. 14. The observations on CIE a* are summarized below:

1. For samples A1 and A4, both before and after carbonation, the CIE a* value rapidly decreases within the first 120 min and continues to decline, albeit at a slower rate, after 2400 min. Given this trend, the RB-stained surfaces of these two samples will be completely cleaned if exposed to UV irradiation for a sufficient duration (e.g., for A6, it is about 300 min). Additionally, sample A1 exhibits much greater drop

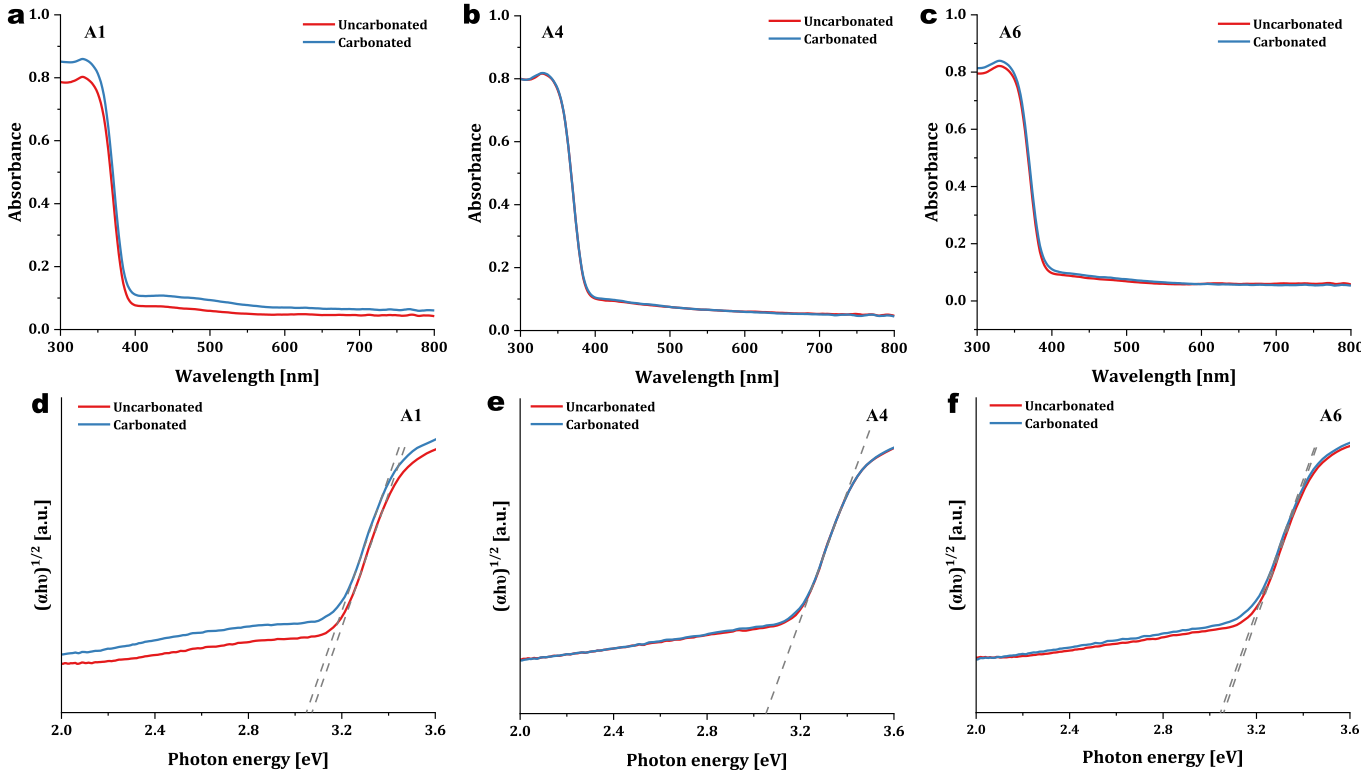

Fig. 12. (a–c) UV-VIS absorbance spectrums and (c–d) Tacu's plots of samples A1, A4, and A6 before and after carbonation.

Table 4
Optical band energy of samples A1, A4, and A6 before and after carbonation.

Sample	Band gap energy [eV]	
	Uncarbonated	Carbonated
A1	3.07	3.04
A4	3.05	3.05
A6	3.05	3.04

in photocatalytic properties compared to sample A4 (the drop in $\varphi_{t=2400min}$ for 20.3 % for sample A1 and 8.0 % for sample A4).

2. Sample A6: Before carbonation, the CIE a* value is slightly below 0 after 600 min, indicating that the RB dye on the A6 surface is completely degraded. This means that sample A6 exhibits superior photocatalytic self-cleaning performance before carbonation, and its intrinsic color is reflected by a CIE a* slightly below 0 (Fig. S3).

To represent the photocatalytic self-cleaning performance at the early and late stages, $\varphi_{t=30min}$ and $\varphi_{t=2400min}$ are adopted. The performance deterioration caused by carbonation in samples A1 and A4 is evident, with different effects on each sample and stage. In addition to microstructural refinement, the decline in photocatalytic performance of these materials could be attributed to the sheltering effect and the occupation of active sites by carbonation products (mainly calcium carbonates) when carbonation occurs on the phases (portlandite and C–S–H phases) around photocatalyst particles [15,45].

According to Table 2, a significantly higher amount of calcium carbonates, especially calcite, is generated in sample A1 compared to sample A6 after carbonation. Although the total content of calcium carbonates in carbonated sample A4 has not been quantified in Table 2, a reasoned conclusion can be made here that carbonated A4 has the lowest amount of calcium carbonates based on the results and analysis provided in the preceding sections. Additionally, the lowest amount of calcite is observed in sample A4 among all carbonated samples, as evident from the XRD patterns and TGA-DTG curves. These results could also explain the distinct variation in photocatalytic properties of samples caused by carbonation.

After carbonation, the performance of samples A1 and A4 decreases by 20.3 % and 8.0 %, respectively, at the late stage. In contrast, the photocatalytic performance of A6 is slightly enhanced at the early stage after carbonation (from about 28.0 % to 29.4 %), which is different from previous studies [15,53]. It could be attributed to the generated γ-Al_2O_3, which has superior catalysis activity and may provide a supporting effect to the overall photocatalytic self-cleaning [47]. A higher self-cleaning efficiency at the early stage indicates a faster removal of surface contaminants, which can prevent the accumulation of pollutants when the building façade is exposed to a persistent source of contamination.

These results highlight the different photocatalytic discoloration processes in three mixes, stemming from distinct underlying kinetics. These kinetics are influenced by the physical and chemical properties, such as microstructure (surface area and pore structure) and phase composition, especially the properties of photocatalytic supporting phases (C–S–H phases and γ-Al_2O_3). Based on the fundamental principles of photocatalysis and the physicochemical results above, short summaries are given as follows:

1. The refinement of microstructure, along with the sheltering effect and the occupation of active sites by carbonation products, are believed to be the major factors affecting the photocatalytic properties of as-prepared materials upon carbonation. The refinement of microstructure influences the mass transport and the amount of active sites, the sheltering effect limits the photon adsorption capacity of photocatalysts, and the occupation of active sites lowers the possibility of initiating photocatalytic reactions.
2. The deterioration of photocatalytic self-cleaning performance caused by carbonation can be limited and/or even compensated by 1) increasing the carbonation resistance of the matrix and 2) regulating

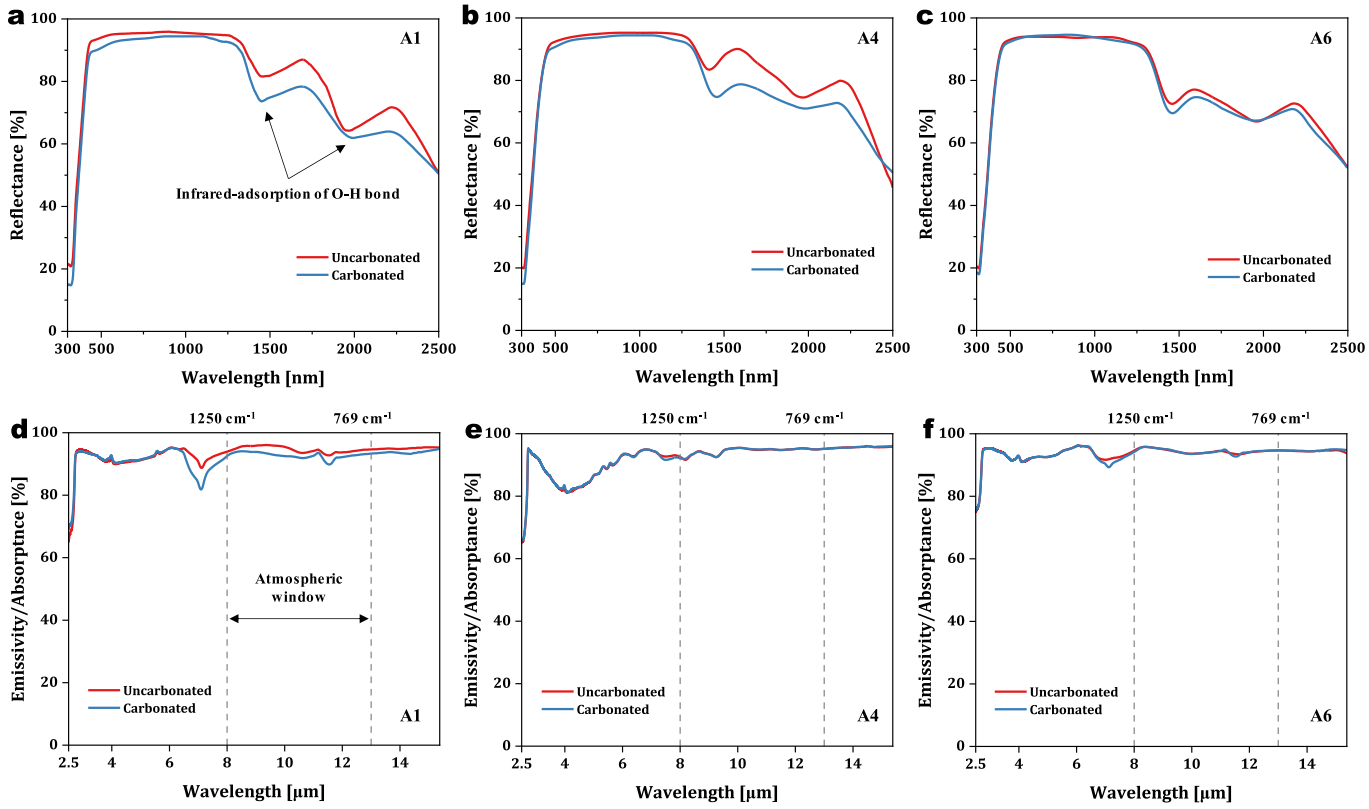

Fig. 13. (a–c) UV-VIS-NIR reflection spectrums and (d–f) Mid-infrared emission spectrums of samples A1, A4, and A6 before and after carbonation.

Table 5
Optical properties of samples A1, A4, and A6 for radiative cooling.

Sample	Solar reflectivity/R_{sun} [%]		Emissivity of atmospheric window/ε_{aw} [%]	
	Uncarbonated	Carbonated	Uncarbonated	Carbonated
A1	91.52	88.73	94.79	92.83
A4	89.27	88.82	93.81	94.00
A6	90.79	88.72	94.02	94.39

the carbonation products with the generation of better photocatalytic support (e.g. γ-Al_2O_3).

3. The photocatalytic kinetics are controlled by distinct factors at different stages. In the early stage, the photocatalytic activity is dominated by the utilization efficiency of photogenerated electron/hole pairs. This efficiency is mainly affected by active sites, which are directly related to surface area and the micromorphology of photocatalytic supporting phases. With the increase in reaction time, the mass transport through the medium capillary pore (10–50 nm) is more important, with the accumulation of reaction products.

The co-use of alumina and nanosilica considerably promotes the incorporation of C–S–H phases. The incorporation of aluminum in foshagite meanwhile provides a useful carbonation mechanism with γ-Al_2O_3 generation against the deterioration of photocatalytic self-cleaning performance. Hence, the hybrid recipe comprising cement (57 wt%), nanosilica (19 wt%), alumina (19 wt%), and titania (5 wt%) in terms of basic photocatalytic properties and durability.

3.6. Outdoor cooling performance

The outdoor measurements commenced at 10:00 a.m. on August 15, 2023, and lasted for one week. These measurements were conducted under various weather conditions, and the results are illustrated in Figs. 15 and 16. Considering the similar optical properties for radiative cooling, A1 was adopted for the outdoor measurement. For this study, both uncarbonated A1 and carbonated A1 were employed.

During the outdoor measurements, it is observed that the interior temperatures inside the test boxes exhibit a wider range of variation compared to the outdoor air temperature. These temperature changes are dominated by solar irradiance. Specifically, a sub-ambient interior cooling of about 4.1 °C lower than the air temperature during the nighttime (8:00 p.m.–8:00 a.m. (next day)), and a near-ambient interior temperature of about 2.5 °C higher than the air temperature during the daytime (8:00 a.m.–8:00 p.m.) are obtained. This finding underscores the effectiveness of mid-infrared thermal radiation provided by the tested aluminosilicate cement paste cooling slices, resulting in an interior cooling effect of approximately 4.1 °C in the given experimental setup. For the 7 d outdoor measurements, overall sub-ambient cooling, with average interior temperatures lower than the outdoor ambient temperature, is observed as shown in Fig. 16a.

Specifically, the sub-ambient cooling is quantified as approximately −1.6 °C for uncarbonated A1 and -1.1 °C for carbonated A1 (Fig. 16a). This observation aligns with the predictions made in **Section 3.4**, where it is anticipated that carbonation would lead to a reduction in radiative cooling performance. The surface temperature measurements also show similar results for different cooling slices. In comparison to a floor made of ordinary cement mortar according to the IR photos in Fig. 16b and c, the prepared aluminosilicate cement pastes, whether carbonated or not, can offer a significant surface cooling effect, reducing the surface temperature by approximately 15.0 °C, indicating considerable energy-saving potential for building cooling.

Additionally, the presence of precipitation, rainwater (on 8/19/2023), is found to impact the radiative cooling performance (Fig. 15). Rainwater can alter the optical properties of the local atmosphere and create a thin water layer above the PE film. These alterations in atmospheric optical properties can limit the thermal radiation exchange

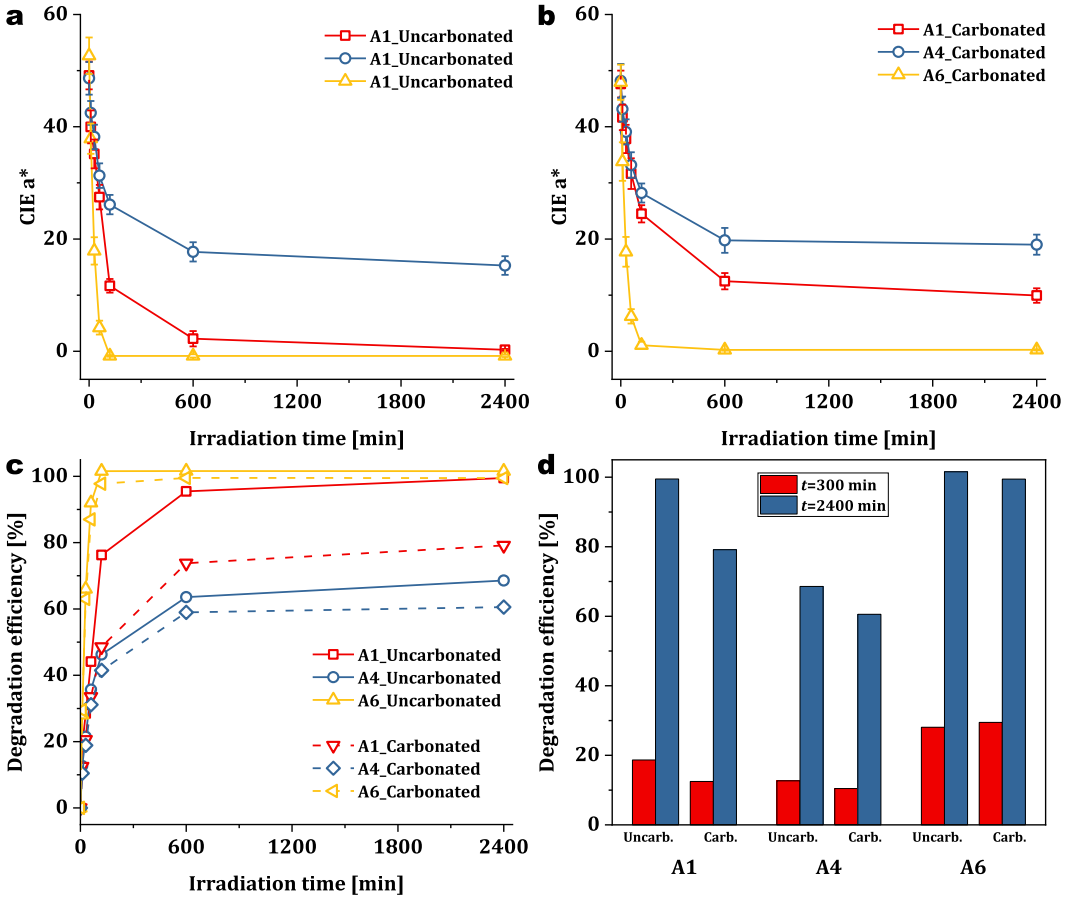

Fig. 14. (a–b) The variation of CIE a*, (c) The variation of discoloration rate, and (d) Discoloration rates at $t = 30$ min and $t = 2400$ min of samples A1, A4, and A6 with UV irradiation.

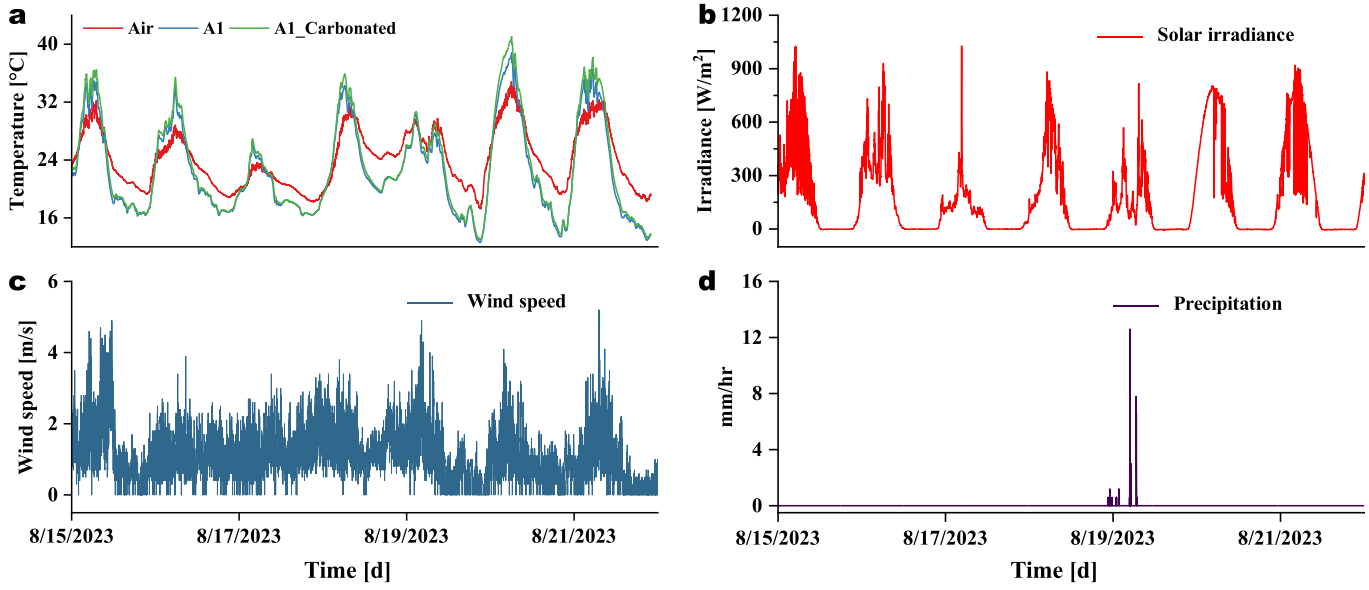

Fig. 15. (a) Interior temperatures, (b) Solar irradiance, (c) Wind speed, and (d) Precipitation during the outdoor measurement.

between the cooling slice and the universe. Moreover, the presence of the water layer significantly affects the thermal conduction between the surface of the PE film and the cooling slice, as well as the surrounding air. Consequently, rainwater has a notable influence on the overall heat exchange between the cooling slice and the air or the environment. These findings highlight the importance of considering environmental conditions, including weather and precipitation, when assessing the radiative cooling performance of materials in real-world outdoor settings.

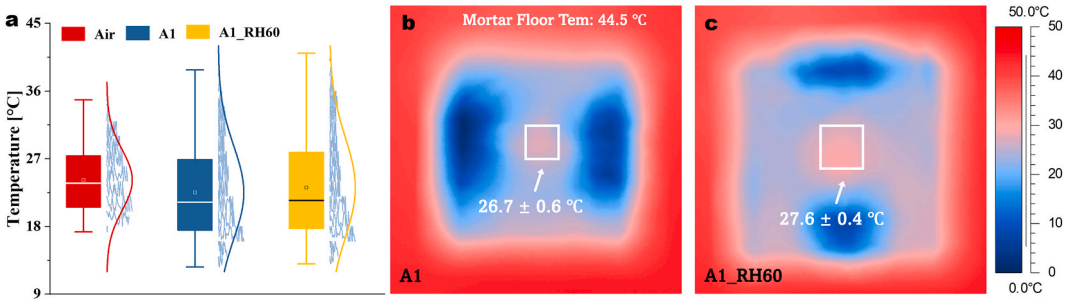

Fig. 16. (a) Box chart of interior temperatures and (b–c) Infrared photos of aluminosilicate cement pastes under sun exposure (03:00 p.m. on Aug/18/2023).

4. Discussions

4.1. Crack formation mechanisms

1. Crack formation upon autoclave curing

Comparing sample A5 with sample A6, the substitution of cement by alumina is found to prevent crack formation when nanosilica is used under autoclave conditions. A similar phenomenon was initially hypothesized to be a result of the incorporation of aluminum into C–S–H, which could increase its alkali binding capacity and limit the pozzolanic reaction with volume expansion [54]. However, the results of this study cannot support the aforementioned hypothesis as the hydrothermal hydration does not follow the kinetics at room temperature. Notably, sample A2, which uses the same silica content as sample A5, does not exhibit visible cracks during the autoclave treatment. The similar reaction degree of silica for samples A2 and A5 is confirmed, according to the XRD analysis as the quartz peak intensity in sample A2 is quite low. Hence, the crack formation and inhibition mechanisms of aluminosilicate cement pastes upon autoclave should consider the synergistic effects of silica source/reactivity and aluminum incorporation.

Cracks generated upon autoclave curing could be attributed to 1) solid volume expansion upon hydrothermal hydration and 2) gas volume expansion with free water gasification. Samples A2 and A5 show similar skeletal densities while sample A5 shows a higher porosity (38.4 % & 32.1 %), which suggests that solid volume change is not the primary reason for the cracking upon autoclave. Therefore, the volume expansion caused by free water gasification is the major reason. The mechanisms for crack formation and inhibition upon autoclave are presented in Fig. 17. Per the model developed by Quercia et al., it is evident that nanosilica particles exhibit a higher water demand compared to an equivalent quantity of micro quartz particles to maintain the workability of cement pastes [55]. Following 1 d of ambient curing, distinct water distribution behaviors are achieved in samples A5 and A2. In the case of

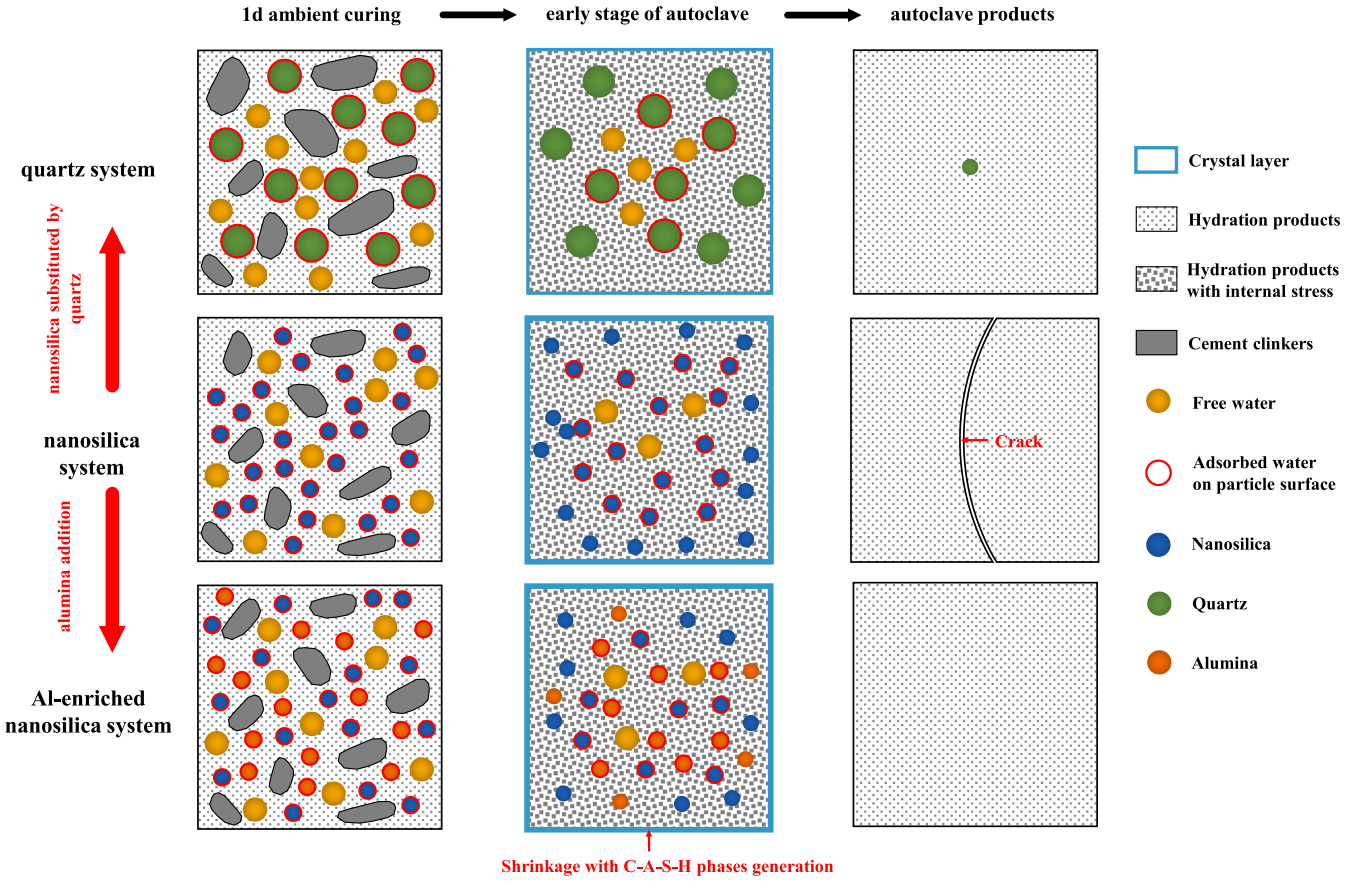

Fig. 17. Schematic of the crack formation mechanisms upon autoclave treatment.

sample A5, more water molecules are physically adsorbed onto the nanosilica particle surfaces, resulting in fewer free water molecules within the pores. Conversely, sample A2 displays the opposite trend. Hence, it is suggested that 1) using amorphous reactive silica with a lower surface area and 2) using better dispersion methods (e.g. pre-ultrasonic dispersion and stronger superplasticizers) to lower water demand, thus limiting the risk of cracking during autoclave.

Upon initiation of autoclave treatment, a series of interconnected processes transpire, guided by heat transfer. Notably, the high-temperature pozzolanic reaction and gasification initiate from the surface and propagate toward the core. This progression accompanies the generation of C–S–H minerals and involves the desorption of physically bound water as well as the gasification of free water. Nanosilica can swiftly establish a denser crystal layer, a process that requires relatively less time compared to quartz. This denser crystal layer subsequently increases the release resistance of gaseous moisture, leading to the generation of internal stress surpassing the matrix's rigid threshold, consequently resulting in cracks.

The incorporation of aluminum yields the formation of C-A-S-H phases within the Al-enriched nanosilica system, contributing to solid volume shrinkage [56]. This shrinkage process effectively compensates for the volume expansion stemming from water gasification, thereby averting the formation of cracks. Therefore, the cracking of cement-silica pastes during autoclave curing can be inhibited by two methods: 1) using the silica source with a lower reactivity and 2) using the reactive aluminum source to promote the C-A-S-H generation.

2. Crack formation upon carbonation

The formation of cracks in cementitious materials due to carbonation is typically associated with the volume expansion of carbonation products, primarily calcium carbonates [18,34]. Research by Morandeau et al. suggests that the transformation of cement hydrates into different calcium carbonates can result in varying degrees of volume expansion [57]. It was believed that calcite caused more significant volume changes than vaterite and aragonite, with amorphous $CaCO_3$ contributing the least. Therefore, based on this understanding and the data provided in Table 2, one would expect that sample A1 should exhibit the most cracks, followed by sample A2, and then sample A6.

However, the experimental results contradict the aforementioned prediction. This inconsistency could be attributed to the different solid volume changes induced by the carbonation of distinct hydrates. Carbonation of amorphous C–S–H (high Ca/Si ratio) in all samples leads to the formation of amorphous C–S–H with a low Ca/Si ratio, amorphous silica gel, and calcium carbonates. Studies have shown that the carbonation of amorphous C–S–H is not considered a significant factor in the cracking of cement-based materials [17,18]. Hence, the carbonation of crystalline C–S–H phases emerges as the primary cause of cracking in aluminosilicate cement pastes upon carbonation in this study.

Based on the phase composition analysis in **Section 3.2.1**, the principal crystalline C–S–H phases in samples A2 and A3 are tobermorite 14 Å and tobermorite 11 Å, respectively. An EDS analysis of the major crystalline phases in uncarbonated samples indicates that tobermorite 14 Å in sample A2 and tobermorite 11 Å in sample A3 have similar Ca/Si ratios of about 0.8 (Fig. 18a). This also suggests the lower quantity of major crystalline C–S–H phase in A3 as it contains lower amount of reacted raw materials than A2.

Meanwhile, as discussed in **Section 3.2.2**, tobermorite 11 Å presents a higher carbonation resistance than other C–S–H phases. These results also highlight that the carbonation of tobermorite induces a substantial solid volume expansion compared to other C–S–H phases. Consequently, the different cracking behaviors upon carbonation of samples A2 and A3 are attributed to the varying solid volume expansion resulting from the carbonation of different amounts and carbonation resistance of tobermorite 11 Å tobermorite 14 Å, as depicted in Fig. 18b.

Therefore, the Ca/Si ratio of raw materials should be taken into account for the durability of cement pastes when quartz is used, as quartz is the direct precursor for tobermorite generation in cementitious systems under autoclave conditions [58]. It is noted not the unreactive quartz in A2 and A3 serves as filler and volume stabilizer, and A3 contains more unreactive quartz. Additionally, the addition of alumina is found to mitigate cracking in aluminosilicate cement pastes upon carbonation, primarily due to the strong calcium bonding capacity of aluminum atoms, which limits the reaction of quartz, therefore the generation of tobermorite.

4.2. Impact of aluminium incorporation

In cementitious systems, various sources of aluminum can impact the properties and performance of materials. These aluminum sources include aluminum-bearing cement clinkers (such as C_3A and C_4AF), clays (e.g., metakaolin), supplementary cementitious materials (e.g., fly

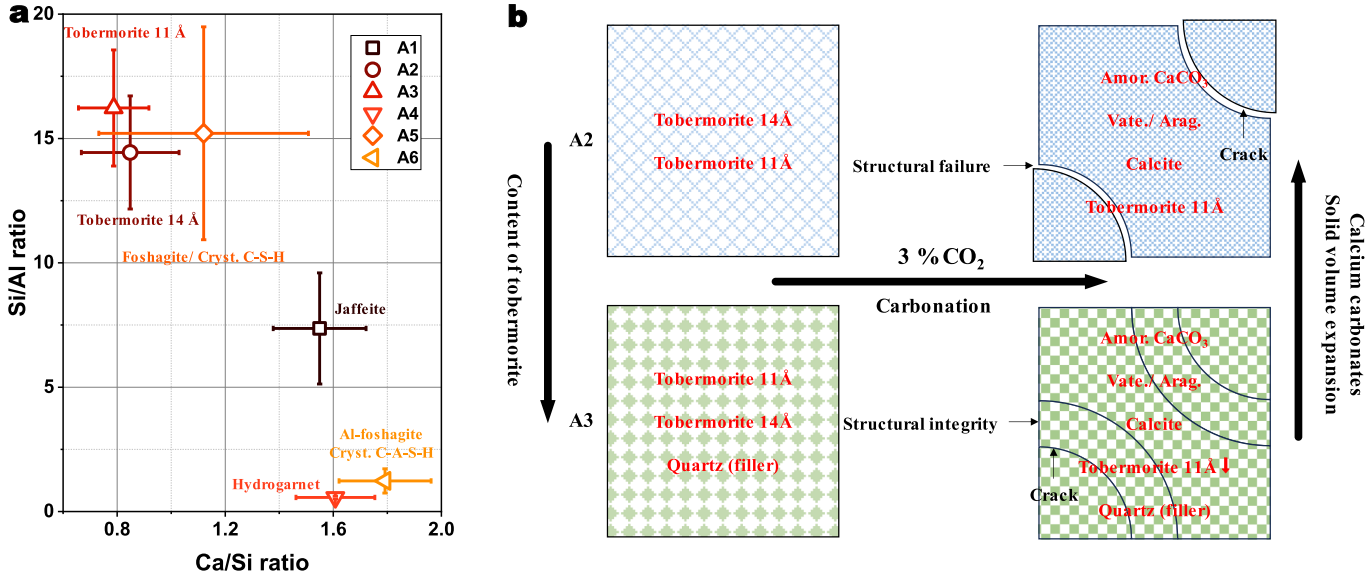

Fig. 18. (a) Ca/Si ratios and Si/Al ratios of the major crystalline phases in uncarbonated samples and (b) Schematic of the crack formation mechanisms upon carbonation.

ash), and alumina. In this study, alumina is chosen as the source of aluminum due to its consistent chemical and physical properties. The results and discussions presented above indicate that aluminum incorporation plays a significant role in shaping the evolution of phase composition and microstructure of aluminosilicate cement pastes during hydrothermal curing and carbonation processes. This, in turn, affects the quality, functional effectiveness, and carbonation durability.

cracking mechanisms are analyzed, as well as the role of alumina addition. The detailed conclusions are drawn as follows:

- With the increase in the CaO/SiO_2 ratio of the cement-quartz binary system, the reaction degree increases but the Basal spacing of tobermorite crystals decreases. It could be attributed to different stoichiometries of Si–O tetrahedrons and H_2O molecules available for coordination with Ca^{2+} ions.
- Alumina facilitates much faster dissolution and reaction kinetics than quartz, and a high Al/Si ratio could promote the generation of hydrogarnet and limit the dissolution/reaction of quartz and the generation of tobermorite, thus contributing to the higher cracking resistance of quartz-based cement pastes upon carbonation.
- The co-use of alumina and nanosilica under the autoclave condition facilitates the generation of microporous C-A-S-H phases. By the carbonation of C-A-S-H minerals, the dealumination achieves the phase transition of Al_2O_3, from the α-phase to the γ-phase. The generated γ-Al_2O_3 could compensate for the drop in photocatalytic self-cleaning performance caused by carbonation.
- Compared with the photocatalytic self-cleaning properties, the optical properties for radiative cooling are more stable upon carbonation, especially ε_{aw}. After carbonation, the developed composites can still provide effective radiative cooling, with a long-term sub-ambient cooling of 1.10 °C (the average of 7 d measurements) and a surface cooling of about 16.0 °C compared with the standard mortar floor.
- The cement/alumina/nanosilica ternary system is determined as optimal in this study, considering the optical properties for radiative cooling, and photocatalytic self-cleaning properties, as well as the producibility and durability.
- The cracking upon autoclave curing could be attributed to the fast reaction kinetics of nanosilica and the volume expansion of water gasification. The co-use of alumina and nanosilica, as well as the addition of unreactive fillers, could eliminate cracking during autoclave treatment.

$$\text{cement} + \text{nanosilica} + Al_2O_3(\alpha) \xrightarrow[\text{autoclave}]{} \underbrace{\overbrace{\text{amor.CASH}}^{\substack{\text{alum. incorp.}\\ \text{solid volume shrinkage}}}}_{\substack{\text{Al.foshagite} + \text{cryst.CASH}\\ \text{photocata. supp.}}} \xrightarrow[\text{carbonation}]{} \underbrace{\overbrace{\text{amor.CASH}}^{\text{alum. incorp.}}}_{\substack{Al_2O_3(\gamma)\\ \text{superior photocata. supp.}}} + C\overline{C}(\text{high}) + SiO_2\ \text{gel(high)} \quad \text{Eq. 4}$$

$$\text{cement} + \text{quartz} + Al_2O_3(\alpha) \xrightarrow[\text{autoclave}]{} \underbrace{\overbrace{\text{hydrogarnet}}^{\substack{\text{carbonation resisting}\\ \text{alum. incorp.}}}}_{} + \underbrace{\text{quartz}}_{\text{low cont}} + \overbrace{\text{CSH phases(low)}}^{\text{carbonatable}} \xrightarrow[\text{carbonation}]{} \underbrace{\overbrace{\text{hydrogarnet}}^{\substack{\text{solid volume stable}\\ \text{alum. incorp.}}}}_{} + \text{quartz} + C\overline{C}(\text{low}) + SiO_2\ \text{gel(low)} \quad \text{Eq. 5}$$

The addition of alumina presents positive impacts on material properties and performance. Here are two scenarios in which alumina is used in combination with other materials to enhance the properties of aluminosilicate cement pastes:

1. Alumina used with nanosilica (Eq. (4)): When alumina is used with nanosilica, it can lead to solid volume shrinkage as C-A-S-H phases are generated. This can limit cracking by compensating for volume expansions caused by the fast reaction kinetics of nanosilica and water gasification under autoclave conditions. The micro-sized homogeneous honeycomb structures produced can serve as excellent photocatalytic supports, enhancing the photocatalytic self-cleaning performance. Additionally, the carbonation of crystalline C-A-S-H phases produces γ-Al_2O_3, which compensates for the decrease in photocatalytic self-cleaning performance caused by changes in microstructure and phase composition upon carbonation.
2. Alumina used with quartz (Eq. (5)): When alumina is introduced alongside quartz, the differences in their dissolution rates lead to the formation of a solution with a much higher AlO_4^{5-}/SiO_4^{4-} mole ratio compared to OPC-based systems. In this Al-enriched system, the AlO_4^{5-} and SiO_4^{4-} monomers are more likely to form hydrogarnet instead of tobermorite. This results in more carbonation-stable phases and fewer carbonation-sensitive phases, thus enhancing the carbonation resistance of the material,

In both scenarios, the addition of alumina plays a critical role in shaping the phase composition and microstructure of aluminosilicate cement pastes, leading to improved material properties and performance, especially the photocatalytic self-cleaning performance and carbonation resistance.

5. Conclusions

To comprehend the impact of carbonation on photocatalytic self-cleaning and radiative cooling properties, as well as the carbonation mechanism of multifunctional cementitious materials. Multifunctional cement pastes are prepared with different silica contents and sources, with and without alumina addition under autoclave conditions. The phase composition, microstructure, optical properties, and photocatalytic self-cleaning performance of as-prepared materials are characterized and analyzed. Onsite outdoor measurements are performed to validate the cooling performance of as-prepared materials. Based on the obtained results, the autoclave-induced and carbonation-induced

CRediT authorship contribution statement

Daoru Liu: Writing – original draft, Methodology, Investigation, Formal analysis, Data curation, Conceptualization. **J.C.O. Zepper:** Methodology, Investigation. **Yuxuan Chen:** Investigation. **Lulu Cheng:** Investigation. **Qingliang Yu:** Writing – review & editing, Supervision, Project administration, Funding acquisition, Conceptualization.

Declaration of competing interest

The authors declare that they have no known competing financial interests or personal relationships that could have appeared to influence the work reported in this paper.

Data availability

Data will be made available on request.

Acknowledgments

This research is supported by the National Natural Science Foundation of China (Grant No. 52178246), China Scholarship Council (No. 202006950045), and Eindhoven University of Technology.

Appendix A. Supplementary data

Supplementary data to this article can be found online at https://doi.org/10.1016/j.cemconcomp.2024.105626.

References

[1] D. Liu, A. Kaja, J.C.O. Zepper, D. Fan, D. Zhang, H.J.H. Brouwers, Q. Yu, Scalable cooling cementitious composites: synergy between reflective, radiative, and evaporative cooling, Energy Build. 285 (2023) 112909, https://doi.org/10.1016/j.enbuild.2023.112909.

[2] B. Zhao, M. Hu, X. Ao, N. Chen, G. Pei, Radiative cooling: a review of fundamentals, materials, applications, and prospects, Appl. Energy 236 (2019) 489–513, https://doi.org/10.1016/j.apenergy.2018.12.018.

[3] Y. ling Song, K.S. Darani, A.I. Khdair, G. Abu-Rumman, R. Kalbasi, A review on conventional passive cooling methods applicable to arid and warm climates considering economic cost and efficiency analysis in resource-based cities, Energy Rep. 7 (2021) 2784–2820, https://doi.org/10.1016/j.egyr.2021.04.056.

[4] J. Liu, Z. Zhou, J. Zhang, W. Feng, J. Zuo, Advances and challenges in commercializing radiative cooling, Mater. Today Phys. 11 (2019) 100161, https://doi.org/10.1016/j.mtphys.2019.100161.

[5] S. Chen, K. Lin, A. Pan, T.C. Ho, Y. Zhu, C.Y. Tso, Study of a passive radiative cooling coating on chemical storage tanks for evaporative loss control, Renew. Energy 211 (2023) 326–335, https://doi.org/10.1016/j.renene.2023.04.141.

[6] J. Mandal, Y. Fu, A.C. Overvig, M. Jia, K. Sun, N.N. Shi, H. Zhou, X. Xiao, N. Yu, Y. Yang, Hierarchically porous polymer coatings for highly efficient passive daytime radiative cooling, Science 362 (2018) 315–319, https://doi.org/10.1126/science.aat9513.

[7] H. Kim, S. McSherry, B. Brown, A. Lenert, Selectively enhancing solar scattering for direct radiative cooling through control of polymer Nanofiber morphology, ACS Appl. Mater. Interfaces 12 (2020) 43553–43559, https://doi.org/10.1021/acsami.0c09374.

[8] T. Lu, E. Solis-Ramos, Y. Yi, M. Kumosa, UV degradation model for polymers and polymer matrix composites, Polym. Degrad. Stabil. 154 (2018) 203–210, https://doi.org/10.1016/j.polymdegradstab.2018.06.004.

[9] A. Baniassadi, D.J. Sailor, G.A. Ban-Weiss, Potential energy and climate benefits of super-cool materials as a rooftop strategy, Urban Clim. 29 (2019) 100495, https://doi.org/10.1016/j.uclim.2019.100495.

[10] N. Yang, Y. Fu, X. Xue, D. Lei, J.G. Dai, Geopolymer-based sub-ambient daytime radiative cooling coating, EcoMat 5 (2023) 1–10, https://doi.org/10.1002/eom2.12284.

[11] G. Chen, Y. Wang, J. Qiu, J. Cao, Y. Zou, S. Wang, D. Jia, Robust inorganic daytime radiative cooling coating based on a Phosphate geopolymer. https://doi.org/10.1021/acsami.0c15799, 2020.

[12] K. Matsui, J. Kikuma, M. Tsunashima, T. Ishikawa, S.Y. Matsuno, A. Ogawa, M. Sato, In situ time-resolved X-ray diffraction of tobermorite formation in autoclaved aerated concrete: influence of silica source reactivity and Al addition, Cement Concr. Res. 41 (2011) 510–519, https://doi.org/10.1016/j.cemconres.2011.01.022.

[13] B. Yuan, C. Straub, S. Segers, Q.L. Yu, H.J.H. Brouwers, Sodium carbonate activated slag as cement replacement in autoclaved aerated concrete, Ceram. Int. 43 (2017) 6039–6047, https://doi.org/10.1016/j.ceramint.2017.01.144.

[14] D. Liu, J.C.O. Zepper, B. Yuan, Y. Chen, Q. Yu, Self-cleaning performance of autoclaved photocatalytic cement pastes: insights into phase composition, microstructure and aluminum incorporation in C–S–H, Ceram. Int. 50 (2024) 5835–5848, https://doi.org/10.1016/j.ceramint.2023.11.394.

[15] D. Liu, A. Kaja, Y. Chen, H.J.H. Brouwers, Q. Yu, Self-cleaning performance of photocatalytic cement mortar: synergistic effects of hydration and carbonation, Cement Concr. Res. 162 (2022) 107009, https://doi.org/10.1016/j.cemconres.2022.107009.

[16] V. Matějka, P. Matějková, P. Kovář, J. Vlček, J. Přikryl, P. Červenka, Z. Lacný, J. Kukutschová, Metakaolinite/TiO2 composite: Photoactive admixture for building materials based on Portland cement binder, Construct. Build. Mater. 35 (2012) 38–44, https://doi.org/10.1016/j.conbuildmat.2012.02.086.

[17] E. Kangni-Foli, S. Poyet, P. Le Bescop, T. Charpentier, F. Bernachy-Barbé, A. Dauzères, E. L'Hôpital, J.-B. d'Espinose de Lacaillerie, Carbonation of model cement pastes: the mineralogical origin of microstructural changes and shrinkage, Cement Concr. Res. 144 (2021) 106446, https://doi.org/10.1016/j.cemconres.2021.106446.

[18] B. Šavija, M. Luković, Carbonation of cement paste: understanding, challenges, and opportunities, Construct. Build. Mater. 117 (2016) 285–301, https://doi.org/10.1016/j.conbuildmat.2016.04.138.

[19] M. Zajac, A. Lechevallier, P. Durdzinski, F. Bullerjahn, J. Skibsted, M. Ben Haha, CO2 mineralisation of Portland cement: towards understanding the mechanisms of enforced carbonation, J. CO2 Util. 38 (2020) 398–415, https://doi.org/10.1016/j.jcou.2020.02.015.

[20] G. Lu, W. She, X. Tong, W. Zuo, Y. Zhang, Radiative cooling potential of cementitious composites: physical and chemical origins, Cem. Concr. Compos. 119 (2021) 104004, https://doi.org/10.1016/j.cemconcomp.2021.104004.

[21] Y. Qin, Y. Zhao, X. Chen, L. Wang, F. Li, T. Bao, Moist curing increases the solar reflectance of concrete, Construct. Build. Mater. 215 (2019) 114–118, https://doi.org/10.1016/j.conbuildmat.2019.04.164.

[22] E. Kangni-foli, S. Poyet, P. Le Bescop, T. Charpentier, A. Dauzeres, E.L. Hopital, J. D. De Lacaillerie, E. Kangni-foli, S. Poyet, P. Le Bescop, T. Charpentier, A. Dauzeres, Calcium alumino-silicates hydrates (C-A-S-H) carbonation kinetics, in: ICCC 2019-15th, Int. Congr. Chem. Cem., Prague, Czech Republic, 2019. https://cea.hal.science/cea-03211966.

[23] K. Garbev, P. Stemmermann, L. Black, C. Breen, J. Yarwood, B. Gasharova, Structural features of C-S-H(I) and its carbonation in air-A Raman spectroscopic study. Part I: fresh phases, J. Am. Ceram. Soc. 90 (2007) 900–907, https://doi.org/10.1111/j.1551-2916.2006.01428.x.

[24] T.F. Sevelsted, J. Skibsted, Carbonation of C-S-H and C-A-S-H samples studied by 13C, 27Al and 29Si MAS NMR spectroscopy, Cement Concr. Res. 71 (2015) 56–65, https://doi.org/10.1016/j.cemconres.2015.01.019.

[25] L. Black, K. Garbev, I. Gee, Surface carbonation of synthetic C-S-H samples: a comparison between fresh and aged C-S-H using X-ray photoelectron spectroscopy, Cement Concr. Res. 38 (2008) 745–750, https://doi.org/10.1016/j.cemconres.2008.02.003.

[26] A.M. Kaja, H.J.H. Brouwers, Q.L. Yu, NOx degradation by photocatalytic mortars: the underlying role of the CH and C-S-H carbonation, Cement Concr. Res. 125 (2019) 105805, https://doi.org/10.1016/j.cemconres.2019.105805.

[27] Z. Liu, W. Meng, Fundamental understanding of carbonation curing and durability of carbonation-cured cement-based composites: a review, J. CO2 Util. 44 (2021) 101428, https://doi.org/10.1016/j.jcou.2020.101428.

[28] X. Liu, P. Feng, Y. Cai, X. Yu, Q. Liu, Carbonation behaviors of calcium silicate hydrate (C-S-H): effects of aluminum, Construct. Build. Mater. 325 (2022) 126825, https://doi.org/10.1016/j.conbuildmat.2022.126825.

[29] R. Mejía de Gutiérrez, M.A. Villaquirán-Caicedo, L.A. Guzmán-Aponte, Alkali-activated metakaolin mortars using glass waste as fine aggregate: mechanical and photocatalytic properties, Construct. Build. Mater. 235 (2020), https://doi.org/10.1016/j.conbuildmat.2019.117510.

[30] D.E. Cadore, C. Angulski da Luz, M.H. Farias de Medeiros, An investigation of the carbonation of alkaline activated cement made from blast furnace slag generated by charcoal, Construct. Build. Mater. 226 (2019) 117–125, https://doi.org/10.1016/j.conbuildmat.2019.07.209.

[31] G173–03: Standard Tables for Reference Solar Spectral Irradiances: Direct Normal and Hemispherical on 37° Tilted Surface, ASTM International, the US, 2003.

[32] P.R. Jubu, F.K. Yam, V.M. Igba, K.P. Beh, Tauc-plot scale and extrapolation effect on bandgap estimation from UV–vis–NIR data – a case study of β-Ga2O3, J. Solid State Chem. 290 (2020) 121576, https://doi.org/10.1016/j.jssc.2020.121576.

[33] International Organization for Standardization (ISO 10678), Fine Ceramics (Advanced Ceramics, Advanced Technical Ceramics) — Determination of Photocatalytic Activity of Surfaces in an Aqueous Medium by Degradation of Methylene Blue, 2010.

[34] M. Auroy, S. Poyet, P. Le Bescop, J.M. Torrenti, T. Charpentier, M. Moskura, X. Bourbon, Comparison between natural and accelerated carbonation (3% CO2): impact on mineralogy, microstructure, water retention and cracking, Cement Concr. Res. 109 (2018) 64–80, https://doi.org/10.1016/j.cemconres.2018.04.012.

[35] B. Lothenbach, D. Jansen, Y. Yan, J. Schreiner, Solubility and characterization of synthesized 11 Å Al-tobermorite, Cement Concr. Res. 159 (2022) 106871, https://doi.org/10.1016/j.cemconres.2022.106871.

[36] P. Yu, R.K. J., Thermal dehydration of tobermorite and jennite, Concr. Sci. Eng. 1 (1999) 185–191.

[37] E. Bonaccorsi, S. Merlino, H.F.W. Taylor, The crystal structure of jennite, Ca9Si6O18(OH)6·8H2O, Cement Concr. Res. 34 (2004) 1481–1488, https://doi.org/10.1016/j.cemconres.2003.12.033.

[38] T. Wei, F. Wei, J. Zhou, Z. Wu, C. Zhang, J. Zhuang, X. Cheng, Formation and strengthening mechanisms of xonotlite in C3S-silica and C2S-silica powder systems under high temperature and pressure, Cement Concr. Res. 157 (2022) 106812, https://doi.org/10.1016/j.cemconres.2022.106812.

[39] T. Wei, X. Cheng, T. Gu, S. Huang, C. Zhang, J. Zhuang, Y. Zheng, The change and influence mechanism of the mechanical properties of tricalcium silicate hardening at high temperature, Construct. Build. Mater. 308 (2021) 125065, https://doi.org/10.1016/j.conbuildmat.2021.125065.

[40] T. Wei, X. Cheng, H. Liu, H. Zhang, L. Zhang, K. Mei, C. Zhang, K. Liu, J. Zhuang, Crystallization of tricalcium silicate blended with different silica powder dosages at high temperature, Construct. Build. Mater. 316 (2022) 125884, https://doi.org/10.1016/j.conbuildmat.2021.125884.

[41] J.M. Rivas-Mercury, P. Pena, A.H. de Aza, X. Turrillas, Dehydration of Ca3Al2(SiO4)y(OH)4(3−y) (0<y<0.176) studied by neutron thermodiffractometry, J. Eur. Ceram. Soc. 28 (2008) 1737–1748, https://doi.org/10.1016/j.jeurceramsoc.2007.12.038.

[42] E. L'Hôpital, B. Lothenbach, G. Le Saout, D. Kulik, K. Scrivener, Incorporation of aluminium in calcium-silicate-hydrates, Cement Concr. Res. 75 (2015) 91–103, https://doi.org/10.1016/j.cemconres.2015.04.007.

[43] B. Lu, S. Drissi, J. Liu, X. Hu, B. Song, C. Shi, Effect of temperature on CO2 curing, compressive strength and microstructure of cement paste, Cement Concr. Res. 157 (2022) 106827, https://doi.org/10.1016/j.cemconres.2022.106827.
[44] Y. Li, W. Liu, F. Xing, S. Wang, L. Tang, S. Lin, Z. Dong, Carbonation of the synthetic calcium silicate hydrate (C-S-H) under different concentrations of CO2: chemical phases analysis and kinetics, J. CO2 Util. 35 (2020) 303–313, https://doi.org/10.1016/j.jcou.2019.10.001.
[45] J. Chen, C. Poon, Photocatalytic cementitious materials: influence of the microstructure of cement paste on photocatalytic pollution degradation, Environ. Sci. Technol. 43 (2009) 8948–8952, https://doi.org/10.1021/es902359s.
[46] R. Prins, On the structure of γ-Al2O3, J. Catal. 392 (2020) 336–346, https://doi.org/10.1016/j.jcat.2020.10.010.
[47] W. Lueangchaichaweng, B. Singh, D. Mandelli, W.A. Carvalho, S. Fiorilli, P. P. Pescarmona, High surface area, nanostructured boehmite and alumina catalysts: Synthesis and application in the sustainable epoxidation of alkenes, Appl. Catal. Gen. 571 (2019) 180–187, https://doi.org/10.1016/j.apcata.2018.12.017.
[48] K. Yanagisawa, X. Hu, A. Onda, K. Kajiyoshi, Hydration of β-dicalcium silicate at high temperatures under hydrothermal conditions, Cement Concr. Res. 36 (2006) 810–816, https://doi.org/10.1016/j.cemconres.2005.12.009.
[49] D. Zhao, Y. Gao, S. Nie, Z. Liu, F. Wang, P. Liu, S. Hu, Self-assembly of honeycomb-like calcium-aluminum-silicate-hydrate (C-A-S-H) on ceramsite sand and its application in photocatalysis, Chem. Eng. J. 344 (2018) 583–593, https://doi.org/10.1016/j.cej.2018.03.074.
[50] D. Liu, J.C.O. Zepper, D. Fan, Q. Yu, Photocatalytic cement-based passive cooling composites: the synergy of radiative cooling and self-cleaning mechanisms, J. Build. Eng. 1446 (2024) 108749, https://doi.org/10.1016/j.jobe.2024.108749.
[51] J.J. Chen, J.J. Thomas, H.F.W. Taylor, H.M. Jennings, Solubility and structure of calcium silicate hydrate, Cement Concr. Res. 34 (2004) 1499–1519, https://doi.org/10.1016/j.cemconres.2004.04.034.
[52] A.S. Farooq, P. Zhang, Y. Gao, R. Gulfam, Emerging radiative materials and prospective applications of radiative sky cooling - a review, Renew. Sustain. Energy Rev. 144 (2021) 110910, https://doi.org/10.1016/j.rser.2021.110910.
[53] Z. Wang, Q.L. Yu, P. Feng, H.J.H. Brouwers, Variation of self-cleaning performance of nano-TiO2 modified mortar caused by carbonation: from hydrates to carbonates, Cement Concr. Res. 158 (2022) 106852, https://doi.org/10.1016/j.cemconres.2022.106852.
[54] S.Y. Hong, F. Glasser, Alkali sorption by C-S-H and C-A-S-H gels, Cement Concr. Res. 32 (2002) 1101–1111, https://doi.org/10.1016/S0008-8846(02)00753-6.
[55] G. Quercia, G. Hüsken, H.J.H. Brouwers, Water demand of amorphous nano silica and its impact on the workability of cement paste, Cement Concr. Res. 42 (2012) 344–357, https://doi.org/10.1016/j.cemconres.2011.10.008.
[56] H. Ye, A. Radlińska, Shrinkage mechanisms of alkali-activated slag, Cement Concr. Res. 88 (2016) 126–135, https://doi.org/10.1016/j.cemconres.2016.07.001.
[57] A. Morandeau, M. Thiéry, P. Dangla, Investigation of the carbonation mechanism of CH and C-S-H in terms of kinetics, microstructure changes and moisture properties, Cement Concr. Res. 56 (2014) 153–170, https://doi.org/10.1016/j.cemconres.2013.11.015.
[58] J. Kikuma, M. Tsunashima, T. Ishikawa, S. Matsuno, A. Ogawa, K. Matsui, M. Sato, In situ time-resolved X-ray diffraction of tobermorite formation process under autoclave condition, J. Am. Ceram. Soc. 93 (2010) 2667–2674, https://doi.org/10.1111/j.1551-2916.2010.03815.x.